High-Pressure Synthesis of *β*- and *α*-In$_2$Se$_3$-Like Structures in Ga$_2$S$_3$

Samuel Gallego-Parra,* Rosario Vilaplana,* Oscar Gomis, Plácida Rodríguez-Hernández, Alfonso Muñoz, Jesus Antonio González, Juan Angel Sans, Catalin Popescu, and Francisco Javier Manjón

Read Online

ACCESS | Metrics & More | Article Recommendations | SI Supporting Information

ABSTRACT: The synthesis of polymorphs of *α′*-Ga$_2$S$_3$ at room temperature on compression/decompression is studied from a joint experimental and theoretical point of view to reveal the nature of their crystalline structures. The results of Raman scattering and X-ray diffraction measurements on these polymorphs have been analyzed supported by theoretical *ab initio* simulations. On compression, *α′*-Ga$_2$S$_3$ undergoes a phase transition above 16 GPa to *β′*-Ga$_2$S$_3$ with a tetradymite-like (*R*-3*m*) structure, isostructural with *β*-In$_2$Se$_3$. On decompression, *β′*-Ga$_2$S$_3$ undergoes a phase transition below 9.0 GPa to *φ*-Ga$_2$S$_3$, which is isostructural with *α*-In$_2$Se$_3$ (*R*3*m*). Raman signatures of symmetry breaking as well as clear structural differences between the pressure dependence of the unit-cell volume per formula unit, zero-pressure axial compressibilities, bulk modulus, and their first pressure derivative between *β′*-Ga$_2$S$_3$ and *φ*-Ga$_2$S$_3$ have allowed us to determine the *R*3*m* nature of *φ*-Ga$_2$S$_3$. The observation of the *R*3*m* phase is also supported by theoretical total energy *ab initio* simulations. This result unveils a pressure-induced paraelectric-ferroelectric *R*-3*m*-to-*R*3*m* transition, like the theoretically predicted temperature-induced transition in several III−VI *B*$_2$*X*$_3$ compounds, which could find use in technological applications. Finally, *φ*-Ga$_2$S$_3$ undergoes a phase transition below 1.0 GPa to *γ*-Ga$_2$S$_3$ with a disordered zincblende (*F*-43*m*) phase, isostructural with *α*-Ga$_2$Se$_3$ and remains metastable at room conditions. Since the disordered zincblende phase of Ga$_2$X$_3$ chalcogenides has also been found upon decompression in *A*Ga$_2$X$_4$ chalcogenides, we discuss the relation between the pressure-induced phase transitions of both Ga$_2$X$_3$ and *A*Ga$_2$X$_4$ compounds.
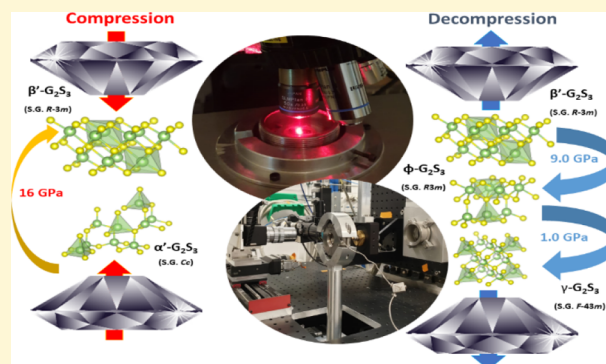
1. INTRODUCTION

Over the last years, many works have reported efforts to crystallize 2D layered structures at room conditions (RC) of the vacancy-disordered, nonlayered, and nonstoichiometric phases of Ga$_2$S$_3$ at high temperature (HT): (i) disordered zincblende (DZ)-like *γ*-Ga$_2$S$_3$ (cubic, space group (s.g.) *F*-43*m*, No. 216, *Z* = 2), at 1130−1180 K; (ii) *α*-Ga$_2$S$_3$ (hexagonal, s.g. *P*6$_1$, No. 161, *Z* = 6); and (iii) wurtzite-like *β*-Ga$_2$S$_3$ (hexagonal, s.g. *P*6$_3$*mc*, No. 186, *Z* = 1), both observed between 1190 and 1300 K.[1−3] To cite just a few examples, *α*-Ga$_2$S$_3$ has been obtained in large-size, 2D layered structures by chemical vapor deposition (CVD),[4] sulfurization,[5] and physical vapor deposition.[6,7] Additionally, 2D layers of *γ*-Ga$_2$S$_3$ have been grown via space-confined CVD,[8] air-spray annealing,[9] and sulfurizing epi-ready GaAs.[10] Even *α′*-Ga$_2$S$_3$ (monoclinic, s.g. *Cc*, No. 9, *Z* = 4 (Figure 1a), the stable polymorph at RC featuring ordered vacancies forming channels, has been obtained as 2D layered structures by gallium-based liquid metal synthesis,[11] exfoliation,[12] and pulsed-laser deposition (PLD),[13] among others. Notably, 2D layered structures with ordered vacancies (*α′*-Ga$_2$S$_3$) and disordered vacancies (*γ*, *α*, and *β* phases) allow conceiving abundant, nontoxic, and eco-friendly layers for a wide variety of applications: nano optoelectronics,[4] photonic chips,[12] electrocatalysis,[14] energy conversion and storage,[15,16] solar cells,[9] gas

sensors,[11,17] laser-radiation detection,[10] and second harmonic generation (SHG).[5,8,17,18]

The above considerations also apply to other Ga-based sesquichalcogenides, like Ga$_2$Se$_3$ and Ga$_2$Te$_3$. The temperature phase diagram of Ga$_2$Se$_3$ shows at room pressure the low-temperature (LT) vacancy-ordered *β*-Ga$_2$Se$_3$ (monoclinic, s.g. *Cc*, No. 9, *Z* = 4, hereinafter called mono-*β*-Ga$_2$Se$_3$) and the DZ phase (Figure 1d) that has been obtained at LT (*α*-Ga$_2$Se$_3$) and at HT (*γ*-Ga$_2$Se$_3$).[19,20] Another phase that can be quenched depending on temperature and Ga/Se ratios is *β*-Ga$_2$Se$_3$ (orthorhombic, s.g. *Imm*2, No. 44, *Z* = 8,[21−25] hereinafter called ortho-*β*-Ga$_2$Se$_3$ (Figure S1) with a vacancy-ordered *α*-II-In$_2$Te$_3$-like structure. Mono-*β*-Ga$_2$Se$_3$ and ortho-*β*-Ga$_2$Se$_3$ differ in the short-range order, ordered zigzag vacancy lines, and (1 0 0) vacancy planes. The ortho phase has been predicted to be much less stable than the mono phase.[22,25,26] Regarding the DZ structure, the *α* (*γ*) structure of Ga$_2$Se$_3$ has been reported at LT
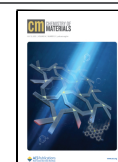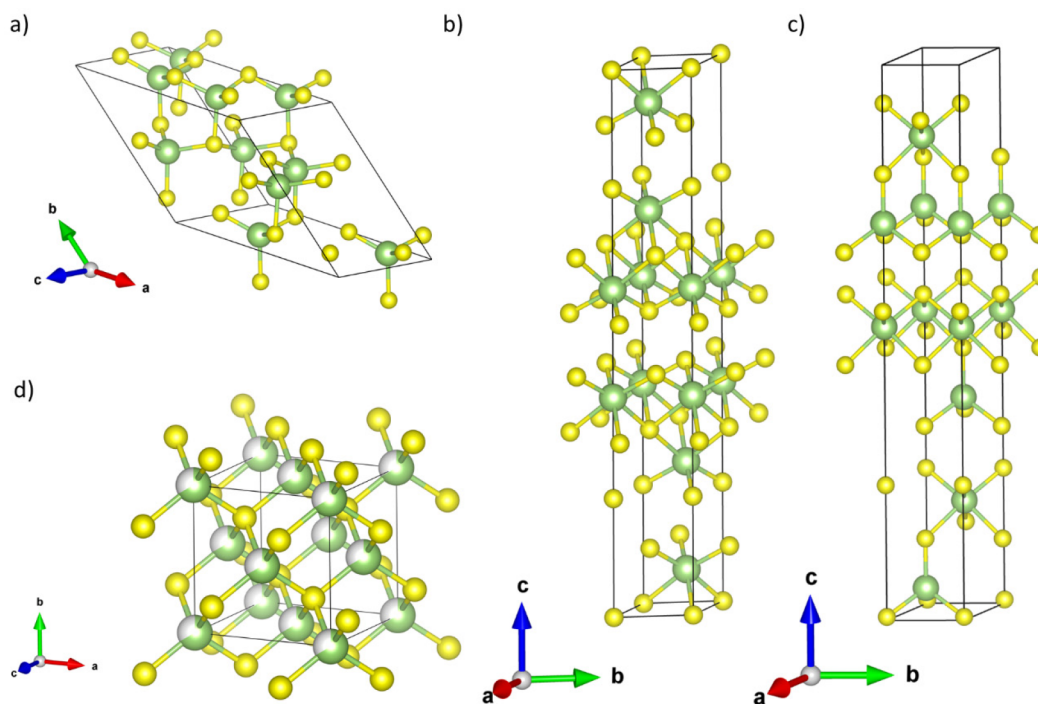
Figure 1. Representation of the structures of Ga_2X_3 compounds involved in this work: (a) monoclinic α'-Ga_2S_3 (s.g. Cc, isostructural to mono-β-Ga_2Se_3 and mono-α-Ga_2Te_3), (b) rhombohedral β'-Ga_2S_3 (s.g. R-$3m$, isostructural to β-In_2Se_3), (c) rhombohedral ϕ-Ga_2S_3 ($R3m$, isostructural to α-In_2Se_3), and (d) DZ γ-Ga_2S_3 (s.g. F-$43m$, isostructural to α-Ga_2Se_3 and β-Ga_2Te_3). Cations and anions are depicted as yellow and green spheres, respectively.

(HT) with a lattice parameter of 5.4222 (5.463 Å).[26,27] This result suggests that both phases are the same one, being that the lattice parameter was affected by thermal expansion. On the other hand, the temperature phase diagram of Ga_2Te_3 only shows β-Ga_2Te_3 with a DZ structure.[28−30] However, α-Ga_2Te_3 (hereinafter, ortho-α-Ga_2Te_3) with a vacancy-ordered α-II-In_2Te_3-like structure has been crystallized by varying Ga/Te ratios at HT.[31,32]

Similarly to defective Ga_2S_3 phases, the defective nonlayered phases of Ga_2Se_3 and Ga_2Te_3 have also been grown in 2D forms: mono-β-Ga_2Se_3 by chemical close-spaced vapor transport,[33,34] low-pressure (LP) CVD,[35] and the sol−gel method;[36] α-Ga_2Se_3 by molecular beam epitaxy (MBE),[37,38] thermal evaporation,[39] and heteroepitaxial growth;[40] and β-Ga_2Te_3 by LP CVD,[35,41] direct synthesis,[42] and PLD.[43] These phases have been used in a number of applications, like in high-performance thermoelectric devices,[41,44,45] phase change memories,[35,43,46] radiation detectors,[25,39] light emitters,[47,48] solar-energy devices,[33,47,49] SHG,[50] and photocatalytic water splitting (PWS) systems.[51]

In an attempt to find additional structures in III−VI B_2X_3 (B = Al,Ga,In; X = S,Se,Te) sesquichalcogenides, recent theoretical works have conducted density functional theory (DFT) and molecular dynamics simulations to evaluate the stability and properties of noncentrosymmetric α-In_2Se_3 (hexagonal, s.g. $R3m$, No. 160, Z = 3, Figure 1c) and centrosymmetric β-In_2Se_3 (hexagonal, s.g. R-$3m$, No. 166, Z = 3, Figure 1b). This latter phase is isostructural with tetradymite-like V−VI sesquichalcogenides, Bi_2Se_3, Sb_2Te_3, and Bi_2Te_3, which are topological insulators at RC.[52] In this context, it is known that α-In_2Se_3 is stable at room temperature (RT)[53] and it undergoes a phase transition (PT) to β-In_2Se_3 at HT.[54−56] Curiously, the α-β PT sequence in In_2Se_3 differs at high pressure (HP) because of the presence of an intermediate β'-In_2Se_3 (monoclinic, s.g. $C2/m$,

No. 12, Z = 3) phase.[57,58] Importantly, ferroelectricity in out-of-plane (OP) and in-plane (IP) polarizations was predicted for the $R3m$ phase.[59] The optimal lattice parameters, electronic band structures, and dynamic stability of α- and β-In_2Se_3 as well as in their isostructural III−VI sesquichalcogenides were also reported. It was commented that the α-In_2Se_3-like structure in these sesquichalcogenides was dynamically stable at RC, unlike the β-In_2Se_3-like structure. Therefore, α-In_2Se_3-like sesquichalcogenides were proposed as 2D ferroelectric materials. Another theoretical work of single- and few-layer α-In_2Se_3-like B_2X_3 (B = Ga,In; X = S,Se) sesquichalcogenides[60] predicted that these layered structures are energetically and mechanically stable, with strong OP and IP ferroelectricity, SHG coefficients, and piezoelectricity. Most extensively, band structures, OP and IP ferroelectricity, as well as analysis of the optical absorption spectrum with quantum and energy efficiencies of ultraviolet, visible, and infrared light absorption, were tabulated in α-In_2Se_3-like sesquichalcogenides to examine the solar-to-hydrogen efficiencies for PWS.[61] All of them were predicted to exhibit an efficiency above 10% and the best of these compounds, In_2Te_3, promises a much higher efficiency above the theoretical efficiency limit (32.1%). Later, molecular dynamics simulations studied the temperature-induced ferroelectric-paraelectric PT associated with the α-β PT in III−VI sesquichalcogenides[62] and spontaneous OP and IP ferroelectricity was found in the α-In_2Se_3-like structure of these compounds at RC. Moreover, the temperatures of the α-β PT were predicted to follow the sequence Al_2X_3 > Ga_2X_3 > In_2X_3. Another theoretical work revised and improved the band gaps of III−VI sesquichalcogenides using DFT+U+V simulations.[63] Finally, recent molecular dynamics simulations of both the α-β and β-α PTs in III−VI sesquichalcogenides[64] predicted that the ferroelectric-paraelectric, α-β PT is fast at HT and assisted by an IP shear

phonon mode, while the β-α PT is hindered by an entropy barrier due to a pseudocentrosymmetric β phase. In summary, theoretical studies have shown a strong interest in the $R3m$ structure of III−VI B_2X_3 sesquichalcogenides for their interesting potential applications.

In this context, the properties of α-In$_2$Se$_3$-like ($R3m$) Ga$_2$S$_3$ has drawn particular attention because several theoretical works suggest that it could form heterojunctions with GaX_2Y (X = S, Se, Y = Se, Te) Janus monolayers, whose band gap and energy levels can be tuned by switching electric dipoles.[65−68] Therefore, 2D band gap-tunable III−VI sesquichalcogenides will stimulate future works devoted to ultrathin 2D photodetection, SHG, piezoelectric devices, emerging quantum applications, PWS, catalytic applications, gas sensors, ultrafast and ultrathin data storage, thermal imaging, energy harvesting, 2D heterojunctions, photovoltaics, and high mobility field-effect transistors.[60,62,64−67]

In Ga$_2X_3$ (X = S, Se, Te) sesquichalcogenides, it has been shown that neither α-In$_2$Se$_3$-like nor β-In$_2$Se$_3$-like structures can be attained at HT or by varying Ga/X ratios. However, there is a controversy regarding whether these phases could be observed in these compounds at HP. X-ray diffraction (XRD) measurements under compression showed a PT to β-In$_2$Se$_3$-like (R-$3m$) Ga$_2$S$_3$ (hereinafter, β'-Ga$_2$S$_3$) around 16 GPa, being the PT assisted by laser heating (LH).[69] However, a PT was found at similar pressures at RT in a study of the structural and vibrational properties of α'-Ga$_2$S$_3$ at HP, i.e., without the need of LH.[70] Similarly, Raman scattering (RS) measurements at RT observed a PT at 11.3 (17.2 GPa) with (and without) He as a pressure-transmitting medium (PTM).[71] In addition, this last work reported two new phases observed in Ga$_2$S$_3$ under decompression below 8.0 and 3.0 GPa, both under hydrostatic and nonhydrostatic conditions, but their structures were neither provided nor suggested. Regarding the HP works focused on Ga$_2$Se$_3$ and Ga$_2$Te$_3$, both DZ-like α-Ga$_2$Se$_3$ and mono-β-Ga$_2$Se$_3$ undergo a reversible HP-PT to a disordered rocksalt (DR) structure above 16 GPa.[72−74] No HP studies of ortho-β-Ga$_2$Se$_3$ have been conducted to our knowledge. On the other hand, DZ-like β-Ga$_2$Te$_3$ was found to undergo a PT to the β-In$_2$Se$_3$ structure (hereinafter, β'-Ga$_2$Te$_3$) above 5 GPa.[75] The reversibility of this PT has not been verified since it has been suggested from resistance measurements at HP. All in all, it can be concluded that there is no report about the observation of the α-In$_2$Se$_3$ ($R3m$) structure in Ga$_2X_3$ sesquichalcogenides either at HT or at HP, to our knowledge. Moreover, it is clear that β'-Ga$_2$S$_3$ and β'-Ga$_2$Te$_3$, isostructural to β-In$_2$Se$_3$ ($R\bar{3}m$), have been only obtained at HP. Noteworthy, a recent work has synthesized β'-Ga$_2$Te$_3$ via nanotectonic compression in bulk glassy Ga−Te alloys from a supercooled liquid after PLD;[46] therefore, this result opens the door to the synthesis of β'-Ga$_2$S$_3$ as a metastable phase at RC.

In this work, we report HP-RS and HP-XRD measurements up to 23.7 and 21.1 GPa, respectively, on α'-Ga$_2$S$_3$ in both under compression and decompression to study the nature and behavior of its HP phases. The structural and vibrational properties of the HP phases of α'-Ga$_2$S$_3$ are jointly analyzed by comparing experimental and theoretical methods. In this way, we address several controversial points from previous works: (1) whether the HP phase of α'-Ga$_2$S$_3$ observed at RT[70,71] is the β' phase observed at HP aided by LH;[68] i.e., whether there is the need of thermal energy[69] to promote the α'-to-β'-Ga$_2$S$_3$ HP-PT around 16 GPa; (2) nature of the soft mode (SM) reported on the RS spectra of β'-Ga$_2$S$_3$,[71] which is not a first-order mode

expected in the tetradymite-like $R\bar{3}m$ structure on the basis of the RS spectra of several tetradymite-like sesquichalcogenides;[52,57] and (3) nature of the two unknown phases observed upon decompression at 8.0 and 3.0 GPa in previously reported HP-RS measurements.[71]

Regarding the first controversial point, we will show that the α'-to-β'-Ga$_2$S$_3$ HP-PT is verified at RT; therefore, it does not require additional thermal energy to occur. In regards to the second point, we will show that the SM of the $R\bar{3}m$ phase can be explained as a second-order Raman mode coming from the A_{1g}^1-E_g^1 combination. Finally, the answer to the third point is the most important contribution of this work. We will show that the first phase observed on decompression from β'-Ga$_2$S$_3$, hereinafter φ-Ga$_2$S$_3$, has the α-In$_2$Se$_3$-like structure (s.g. $R3m$). The existence of the α-In$_2$Se$_3$-like structure in a Ga-based sesquichalcogenide is here experimentally reported for the first time to our knowledge. More importantly, this result implies the existence of a pressure-induced paraelectric-ferroelectric β'-φ phase transition, similar to the predicted temperature-induced ferroelectric-paraelectric α-β-In$_2$Se$_3$-like PT in all III−VI sesquichalcogenides,[62,64] thus connecting PTs either at HP or at HT in these compounds. This result opens new possibilities for Ga$_2$S$_3$ to design cheap, nontoxic, nonrare-earth, and abundant-element-based devices for SHG, PWS, ferroelectric, pyroelectric, and piezoelectric applications. Moreover, it will guide further works devoted on other III−VI sesquichalcogenides to synthesize α- and β-In$_2$Se$_3$-like structures not only at HP but also at RC via existing or emerging 2D materials synthesis methods[9,15,16,66,76−78] or by PLD as β'-Ga$_2$Te$_3$ was recently obtained.[46] Finally, we will propose that the second phase observed on decompression shows a DZ structure and therefore is identified with the γ-Ga$_2$S$_3$ phase observed at HT. Since the DZ-like phase has been already observed on the downstroke in ternary ordered-vacancy compounds (OVCs), like AGa$_2X_4$ compounds (A = Zn,Cd,Hg; X = S,Se), with original defective chalcopyrite (DC) and defect stannite (DS),[79,80] we have reformulated the PT sequence of these ternary OVCs at HP.[81] In this way, we propose a new PT diagram of OVCs at HP that include the family of binary Ga$_2X_3$ compounds and establish that the presence of vacancies and their pressure-induced disorder connects both the LP and HP phases in both families of compounds. Therefore, this work allows us to understand the behavior of III−VI sesquichalcogenides at HP as well as their relation to ternary OVCs at HP.

2. EXPERIMENTAL DETAILS

α'-Ga$_2$S$_3$ and α-In$_2$Se$_3$ powders were obtained from the supplier Alfa Aesar, with high purity (99.99%). For both HP-RS and HP-XRD measurements, α'-Ga$_2$S$_3$ powders were placed in a 150-μm-diameter hole made in an Inconel gasket. A membrane-type diamond-anvil cell (DAC) with a 400-μm-diameter diamond culet was employed. A 4:1 methanol−ethanol (M−E) mixture and silicon oil (S) were used as PTM in HP-RS measurements, while M−E was used in HP-XRD measurements.

Unpolarized HP-RS measurements on α'-Ga$_2$S$_3$ at RT up to 23.7 (run-1) and 27.6 (run-2) GPa with M−E as a PTM as well as the RS measurement of α-In$_2$Se$_3$ at RC were collected with a LabRAM HR UV Raman microspectrometer, equipped with a thermoelectrically cooled CCD camera, with a spectral resolution better than 2 cm^{-1}. Unpolarized HP-RS measurements on α'-Ga$_2$S$_3$ at RT up to 60.0 (run-3) and 29.2 (run-4) GPa with S as a PTM were collected with a T64000 Horiba Raman microspectrometer, equipped with a nitrogen cooled CCD camera, with a spectral resolution better than 2 cm^{-1}. Excitation of all RS signals was performed using the He:Ne line (632.8 nm) with a power below 1 mW. The ruby luminescence method was
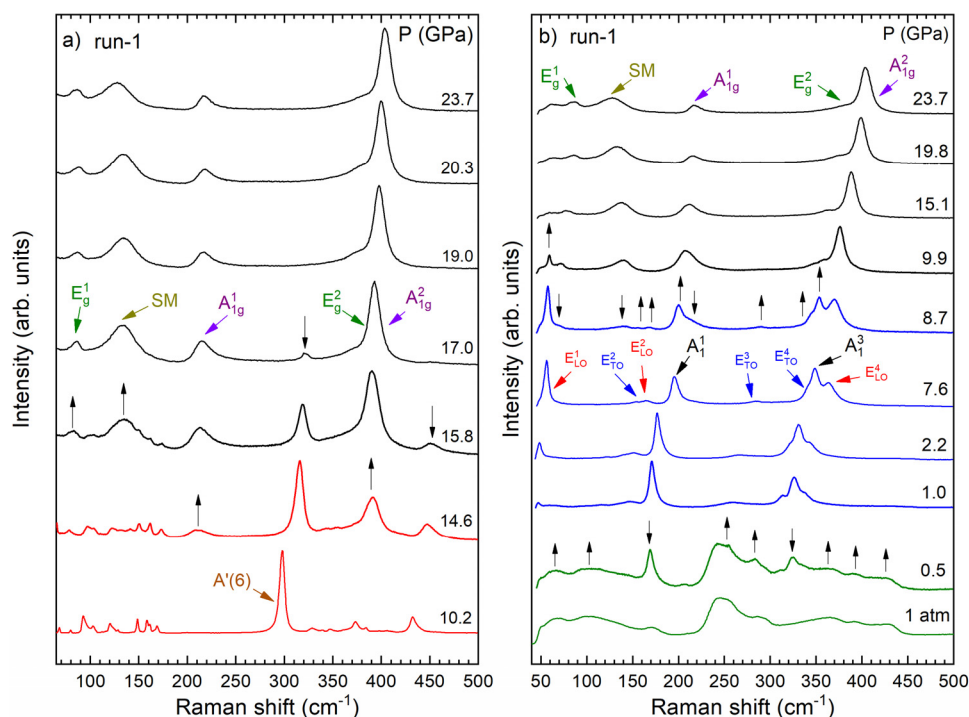
Figure 2. Selected normalized Raman spectra of α'-Ga_2S_3 (run-1) on upstroke (a) and downstroke (b). Down and up arrows indicate the disappearance/emerging of peaks under both compression and decompression. Red, black, blue, and green colors represent the α', β', φ, and γ phases, respectively. For the sake of clarity, only the most intense Raman mode, the A'(6), of α'-Ga_2S_3 is marked in panel a. The reader is referred to our previous work (ref 70) for further information about the pressure dependence of the Raman-active modes of α'-Ga_2S_3. All the observed Raman-active modes have been labeled in β'-Ga_2S_3 and φ-Ga_2S_3. The soft mode in β'-Ga_2S_3 is labeled as the SM mode.

used to determine the pressure in all HP-RS measurements.[82] Raman peaks have been fitted to Voigt profiles with the Gaussian line width fixed to the experimental setup resolution (1.6 cm^{-1}).[83]

Angle-dispersive powder HP-XRD measurements on α'-Ga_2S_3 at RT up to 21.1 GPa were performed at the BL04-MSPD beamline of the ALBA Synchrotron, employing a monochromatic X-ray beam with λ = 0.4246 Å focused to 20 × 20 μm^2 (full width half-maximum).[84] The pressure calibration inside the hole was determined using the equation of state (EoS) of copper.[85] The X-ray beam was focused by Kirkpartrick−Baez mirrors, and images were collected using a Rayonix SX165 CCD detector located at 240 mm from the sample. Two-dimensional diffraction images integrated into one-dimensional profiles of intensity versus 2θ and the calibration using standard LaB$_6$ were performed with Python-based Dioptas software.[86] The Le Bail method was employed in our refinements with GSAS-II software.[87]

3. THEORETICAL DETAILS

Density functional theory (DFT)[88] calculations of β'- and φ-Ga_2S_3 have been carried out with the Vienna Ab-initio Simulation Package (VASP).[89] The projected augmented wave (PAW) potentials[90,91] have been employed to describe valence electrons of Ga (4s^{2}3d^{10}4p^1) and S (3s^{2}3p^4) atoms, considering the full nodal character of the all-electron charge density in the core region but with an affordable basis-set. A plane-wave kinetic-energy cutoff of 380 eV was defined for both β'- and φ-Ga_2S_3 to achieve highly converged results. The exchange-correlation energy was described with the generalized gradient approximation (GGA) of Perdew−Burke−Ernzenhof revised for solids (PBEsol).[92] In order to take into account the weak van der Waals interactions, we also achieve simulations with the PBE functional[93] including the Grimme-D3 dispersion correction.[94] Calculations were performed with dense special k-meshes of 10 × 10 × 10 for β'-Ga_2S_3 and 6 × 6 × 6 for φ-Ga_2S_3,

primitive cells. The simulations provide a data set of volumes, energies, and pressures (from the stress tensor), by fully optimizing the cell parameters and the atomic positions of the structures at selected volumes. For the optimized structures, the Hellmann−Feynman forces were below 0.006 eV/Å per atom, and the deviations of the stress tensor from the diagonal hydrostatic form were smaller than 0.1 GPa.

Lattice-dynamic calculations were performed at the zone center (Γ-point) of the Brillouin zone for Ga_2S_3 employing the direct force-constant approach.[89,95] The transversal optical (TO) modes of β'-Ga_2S_3 and both TO and longitudinal (LO) modes of φ-Ga_2S_3 were analyzed, using a 2 × 2 × 2 supercell in order to include the nonanalytical corrections due to the long-range interaction of the electric field.

Additional simulations have been carried out for several phases of Ga_2Se_3 and Ga_2Te_3, employing the unit cell, with PAW pseudopotentials and the GGA-PBEsol approximation, as for Ga_2S_3. The plane-wave kinetic-energy cutoff was 400 eV. In the case of the mono-β-, ortho-β-, β'-, and φ-Ga_2Se_3, dense special k-meshes of 4 × 4 × 2, 8 × 6 × 2, 9 × 9 × 2, and 9 × 9 × 2, respectively, were used. Finally, for the simulations of mono-α-, ortho-α-, β'-, and φ-Ga_2Te_3, isostructural with the above-mentioned Ga_2Se_3 structures, the special k-meshes were 4 × 4 × 2, 8 × 6 × 2, 9 × 9 × 2, and 9 × 9 × 2.

4. RESULTS

4.1. Vibrational Study under Compression and Decompression. *4.1.1. Compression.* As has been commented on in section 2, four runs of HP-RS measurements have been performed on α'-Ga_2S_3 at RT. For simplicity, we show in Figure 2 only the upstroke and downstroke of run 1. HP-RS spectra on the upstroke of runs 2, 3, and 4 can be seen in panels a,
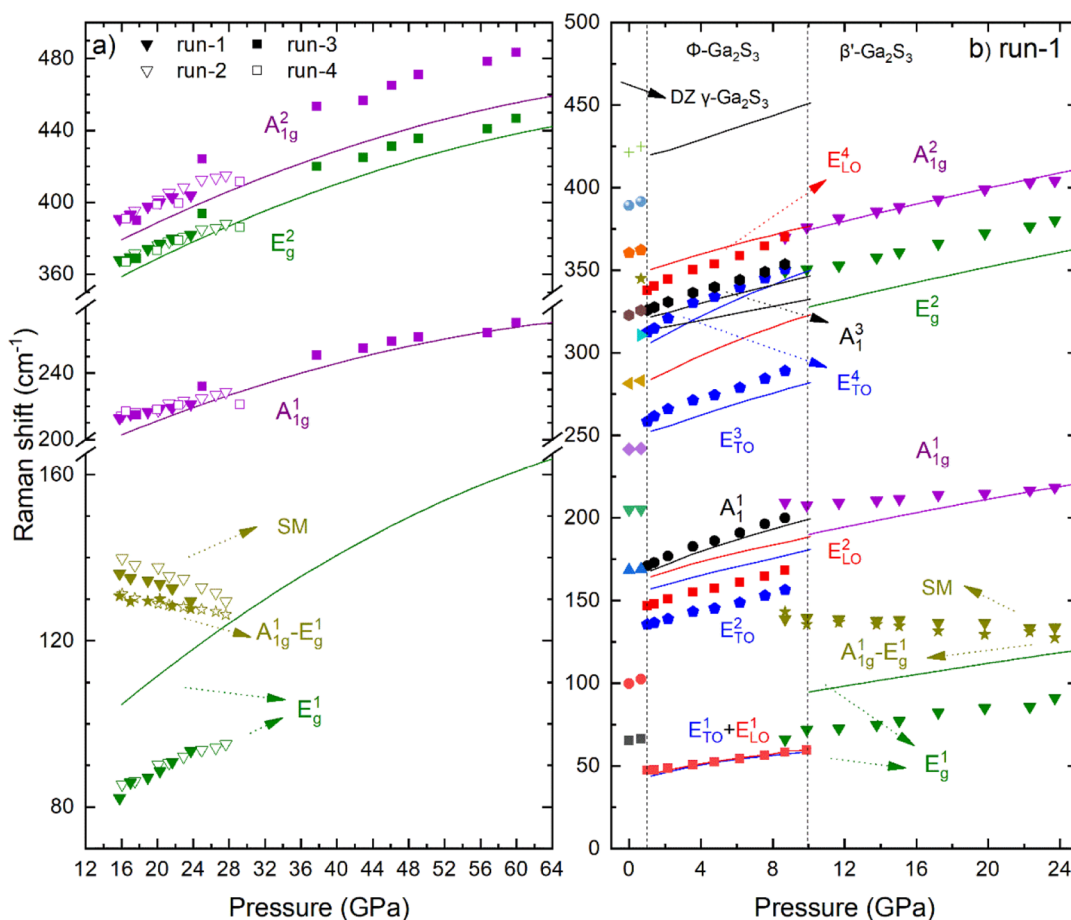
Figure 3. Experimental (symbols) and theoretical (solid lines) pressure dependence of Raman frequencies of (a) β'-Ga$_2$S$_3$ on the upstroke (all runs) and (b) β', φ, and γ phases on the downstroke (run-1). The dotted vertical lines in panel b indicate the phase transition pressures on the downstroke. Both in panels a and b, the experimental frequency of the $A_{1g}^1(\Gamma) - E_g^1(\Gamma)$ difference mode is labeled with hollow star symbols to compare with the SM mode. Black, blue, and red solid lines refer to the theoretical pressure dependence of the frequencies of the A_1, E_{TO}, and E_{LO} modes of φ-Ga$_2$S$_3$ in panel b, respectively. The reader is referred to ref 70 for further information about pressure dependence of the Raman frequencies of α'-Ga$_2$S$_3$.

Table 1. Theoretical and Experimental Frequencies (cm^{-1}), Pressure Coefficients a_1 (in cm^{-1}/GPa) and a_2 (in 10^{-2} cm^{-1}/GPa^2) of the Raman-Active Modes of β'-Ga$_2$S$_3$ (from Run-1 to Run-4) and φ-Ga$_2$S$_3$ (Only for Run-1)[a]

β'-Ga$_2$S$_3$	theoretical			experimental			φ-Ga$_2$S$_3$	theoretical			experimental		
mode	ω_0	a_1	a_2	ω_0	a_1	a_2	mode	ω_0	a_1	a_2	ω_0	a_1	a_2
E_g^1	105.3(2)	1.7(2)	−0.96(4)	84(1)^c	1.5(3)^c	−3.2(4)^c	E_{TO}^1	42.6(4)	2.9(1)	−11.2(1)			
							E_{LO}^1	44.0(3)	2.7(1)	−10.2(1)	47(1)	1.7(2)	−3.5(3)
SM				138(2)^c	−0.4(2)^c	−6(2)^c	E_{TO}^2	155.7(3)	3.2(1)	−5.0(1)	136(2)	2.6(3)	1.1(4)
							E_{LO}^2	163.2(3)	3.5(1)	−7.2(1)	147(2)	3.0(2)	−3.0(3)
$A_{1g}^1 - E_g^1$	98.2(2)	0.4(1)	−0.48(2)	129(1)^c	−0.2(2)^c	−0.5(2)^c	A_1^1	166.5(3)	4.6(1)	−10.6(1)	171(1)	4.3(3)	−9.0(1)
A_{1g}^1	203.3(2)	2.1(2)	−1.48(1)	214(3)^c	1.3(3)^c	−3.6(4)^c	E_{TO}^3	251.3(1)	3.8(1)	−4.6(1)	260(3)	4.0(1)	−9.0(1)
				214(1)^d	1.6(1)^d	−2.8(4)^d	E_{LO}^3	282.1(3)	5.8(1)	−13.0(1)			
							E_{TO}^4	304.2(3)	6.3(1)	−13.0(1)	313(2)	6.8(4)	−25.7(4)
E_g^2	343.6(3)	2.4(1)	−1.49(1)	366(6)^c	2.2(3)^c	−4(3)^c	A_1^1	314.0(1)	1.9(3)	1.4(1)			
				366(1)^d	2.7(4)^d	−4.4(2)^d	A_1^3	320.9(1)	3.1(4)	−2.6(1)	326(1)	3.7(3)	−3.0(4)
A_{1g}^2	390 (1)	2.5(1)	−1.6(3)	390(3)^c	3.0(4)^c	−11.3(3)^c	E_{LO}^4	349.5(2)	3.5(1)	−5.2(1)	338(1)	4.2(5)	−2(1)
				389(3)^d	3.4(4)^d	−5.2(4)^d	A_1^4	419.3(2)	3.3(1)	1.9(1)			

[a]Pressure dependence of the mode frequencies has been fitted to $\omega_i = \omega_{io} + a_1(P - P_0) + a_2 P(P - P_0)^2$, where P_0 is the transition pressure. Theoretical P_0 for the β' and φ phases are fixed to 16 and 1 GPa, respectively. Experimental P_0 are indicated in the table footnotes. M−E, methanol−ethanol; S, silicon oil; P_0, transition pressure. ^{c}Average parameters between run-1 and run-2 (M−E, run-1 $P_0 = 15.8$ and 1 GPa for the β' and φ phases, respectively, and run-2 $P_0 = 15.8$ GPa for β'-Ga$_2$S$_3$). ^{d}Average parameters between run-3 and run-4 (S, run-3 $P_0 = 17.7$ GPa and run-4 $P_0 = 14.8$ GPa for β'-Ga$_2$S$_3$).

b, and c, respectively, of Figure S2 in the Supporting Information. In Figure 2, we observe the continuous

disappearance of the most intense mode (A′(6)) of the LP phase α'-Ga$_2$S$_3$ that can be observed up to 17.0 GPa. Such a
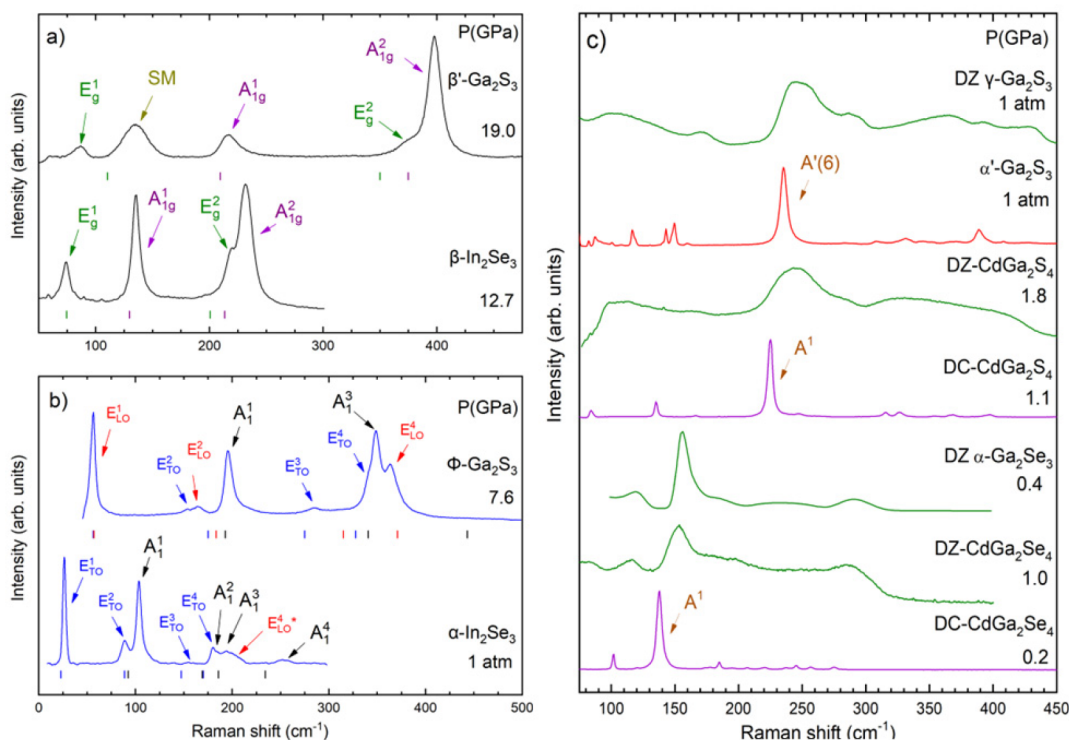
Figure 4. Comparative RS spectra at selected pressures of (a) β'-Ga_2S_3 and β-In_2Se_3 (from ref 57) with s.g. R-$3m$, (b) φ-Ga_2S_3 and α-In_2Se_3 (at 1 atm) with s.g. $R3m$, and (c) DZ γ-Ga_2S_3 and α'-Ga_2S_3 (from ref 70), DZ and DC-$CdGa_2S_4$ (from ref 79), DZ α-Ga_2Se_3 (from ref 74), and DZ and DC-$CdGa_2Se_4$ (from ref 80). Vertical ticks represent the theoretical frequencies at the selected pressures of the different phases shown in panels a and b.

mode corresponds to the breathing mode, the vibrations of S atoms toward the center of the channels that are characteristic of this ordered-vacancy compound (OVC).[70] We refer the reader to ref 70 for further information about the pressure dependence of the Raman-active modes of α'-Ga_2S_3.

In Figure 2, new Raman modes coming from the HP phase of α'-Ga_2S_3 start appearing at 14.6 GPa and are all observed around 80, 140, 220, 380, and 390 cm^{-1} at 15.8 GPa. The same changes in the RS spectra are also observed in runs 2, 3, and 4 at 16.1, 17.7, and 14.8 GPa, respectively (Figure S2). The selected RS spectra of the HP phase of α'-Ga_2S_3 on the upstroke between 15.8 and 23.7 GPa (Figure 2a) resemble those already reported (both with and without He as a PTM).[71] Note that we have observed a low-frequency mode around 80 cm^{-1} that previous HP-RS measurements (made above 100 cm^{-1}) did not report. Despite this drawback, Yang et al.[71] assumed the s.g. R-$3m$ for this HP phase; i.e., they identified it with the β'-Ga_2S_3 observed in previous HP-XRD measurements.[69]

To verify whether the modes of the HP phase of α'-Ga_2S_3 can be explained with the s.g. R-$3m$, we have calculated the theoretical pressure dependence of the Raman frequencies in β'-Ga_2S_3. According to group theory, 15 modes are predicted for the centrosymmetric R-$3m$ phase, 3 acoustic ($A_{2u} + E_u$) and the remaining 12 optical ($2E_g(R) + 2A_{1g}(R) + 2E_u(IR) + 2A_{2u}(IR)$) modes are either Raman-active (R) or infrared-active (IR). In this work, a superindex has been added to each mode in increasing frequency to distinguish among them. The theoretical Raman-active frequencies are plotted together with the experimental ones of the four runs in Figure 3a. Moreover, theoretical and experimental zero-pressure frequencies and their pressure coefficients are summarized in Table 1. The nice comparison of the theoretical and experimental zero-pressure frequencies and pressure coefficients has allowed us to identify

in the HP phase of α'-Ga_2S_3 all the four first-order Raman-active modes (E_g^1, A_{1g}^1, E_g^2, and A_{1g}^2) characteristic of the s.g. R-$3m$ (see Figure 2a and Figure 3a). Therefore, we have verified that β'-Ga_2S_3 is the HP phase of α'-Ga_2S_3 and that it can be obtained at RT without LH. Further details of the structural properties of β'-Ga_2S_3 upon compression will be given in the next section.

Additional support to our assignment has been obtained from the comparison of the HP-RS spectra of β'-Ga_2S_3 and that of β-In_2Se_3 from ref 57 at 19.0 and 12.7 GPa, respectively (Figure 4a). Both RS spectra show a relatively good agreement if we consider the different masses of Ga, In, S, and Se. The main difference between the RS spectra of β'-Ga_2S_3 and β-In_2Se_3 is the appearance of an extra mode in β'-Ga_2S_3 located at around 140 cm^{-1}. This mode, called the SM band, was also observed in previous HP-RS measurements,[71] but no explanation for this mode was reported despite this peak does not appear in the RS spectra of binary sesquichalcogenides with a tetradymite-like structure.[52,57]

Curiously, the SM mode of β'-Ga_2S_3 shows a redshift with increasing pressure (see Figures 2a, Figure 3a, and Figure S2) that does not agree with the blueshift shown by the four first-order Raman-active modes typical of the tetradymite-like III−VI and V−VI sesquichalcogenides.[52,57] In fact, the SM of β'-Ga_2S_3 is not compatible with either Raman-active modes of E_g or A_{1g} symmetries or with IR-active modes of E_u or A_{2u} symmetries, according to our simulations. Instead, we propose that the SM mode is a second-order Raman-active mode related to the $A_{1g}^1 - E_g^1$ difference combination along the Brillouin zone (see Table 1). This hypothesis is supported by the comparison of the experimental frequencies and pressure coefficients of the SM mode and the $A_{1g}^1(\Gamma) - E_g^1(\Gamma)$ combination (see Figure 3a,b. The slight frequency shift between the experimental $A_{1g}^1(\Gamma) - E_g^1(\Gamma)$ combination and the experimental SM mode is likely caused by

the participation of phonons of the A_{1g}^1 and E_g^1 branches outside the Γ point. On the other hand, the theoretical $A_{1g}^1(\Gamma) - E_g^1(\Gamma)$ combination shows a larger deviation from the experimental $A_{1g}^1(\Gamma) - E_g^1(\Gamma)$ combination because of the large overestimation of the theoretical E_g^1 mode frequency with respect the experimental one in our PBEsol calculations. In this sense, it is known that PBEsol calculations tend to overestimate the frequency of the lowest-frequency (interlayer) vibrational modes in vdW layered materials that are related to shear vibrations between neighbor layers due to the underestimation of the c lattice parameter.[96,97] However, we must note that the large overestimation of the E_g^1 mode frequency in β'-Ga$_2$S$_3$ is also found in calculations using the PBE-D3 functional (Figure S3), which additionally underestimates the frequencies of E_g^2 and A_{1g}^2 modes (Figure S3) in a larger extent than calculations using the PBEsol functional.

In regards to the origin of the SM mode in β'-Ga$_2$S$_3$, we can speculate that it is likely due to the existence of a considerable structural defect. Such defects are likely due to the reconstructive nature of the HP-PT, especially between a layered and a nonlayered phase,[98] as it is the case of the α' (Cc) and β'($R\bar{3}m$) phase in Ga$_2$S$_3$. Since the SM mode could be related to defects present in layered β'-Ga$_2$S$_3$, we may wonder whether the α'-to-β' PT would require an extra energy (thermal energy) contribution to overcome the energy barrier between both phases and relax the pressure gradient inside the hole, as Lai et al. suggested from their HP study where β'-Ga$_2$S$_3$ was obtained after applying LH.[69] In this context, our HP-RS measurements (with M—E and S as PTMs) and those reported by Yang et al. (with He and without PTM)[71] suggest that the α'-to-β' HP-PT occurs at RT without the need of LH. Note that Yang et al., who performed HP experiments without PTM;[69] i.e., under more nonhydrostatic conditions than using LiF plates as Lai et al. used in its HP-XRD measurements,[68] reproduced the α'-to-β' PT with a coexistence of both phases between 17.2 and 19.3 GPa. Therefore, α'-Ga$_2$S$_3$ turns into β'-Ga$_2$S$_3$ at HP without the need of LH between 11.3 and 19.3 GPa depending on the hydrostatic conditions. However, it must be commented that an energy contribution via LH could favor the α'-to-β' PT, thus providing a phase with lower structural defects. In this context, it remains to be seen whether the SM appears in such synthesis conditions.

To shed light on the dynamic stability of β'-Ga$_2$S$_3$ at HP and the possible effect of temperature on the α'-to-β' HP-PT, we have calculated the phonon dispersion curves of β'-Ga$_2$S$_3$ at 17.6 and 18.6 GPa (Figure S4a,b). We observe an imaginary phonon at the high symmetry point T at 17.6 GPa (Figure S4a). This result is different to that reported in ref 64 (Figure S11d), which show imaginary phonons at all high symmetry paths, as it has been observed in the β-In$_2$Se$_3$ at RC.[62,64] Pressure dynamically stabilizes the $R\bar{3}m$ structure in Ga$_2$S$_3$ since at 18.6 GPa (Figure S4b) no imaginary phonons appear. Since experimentally the R-$3m$ phase appears from 12 GPa on at RT depending on the hydrostatic conditions as exemplified in this work and in refs 69 and 71 our lattice dynamics calculations at 0 K suggest that temperature also plays a role in stabilizing this phase at RT at smaller pressures than theoretically predicted to be stable. Therefore, we conclude that the R-$3m$ phase is reached in Ga$_2$S$_3$ at RT and HP in the same way as the $R\bar{3}m$ phase is found in In$_2$Se$_3$ at RT and HP.[99]

4.1.2. Decompression. On decompression from above 20 GPa, we have observed that all RS spectra correspond to β'-Ga$_2$S$_3$ down to 10 GPa (see Figure 2b) and there is a good

agreement between the pressure dependence of the experimental and theoretical Raman frequencies in the whole pressure range (Figure 3b). Several changes in the RS spectrum can be observed below 10 GPa (see Figure 2b). A new peak arises in the left side of the E_g^1 mode at 9.9 GPa, thus suggesting a first PT (from β'-Ga$_2$S$_3$ to φ-Ga$_2$S$_3$) on decompression. Between 8.7 and 7.6 GPa, the E_g^1, A_{1g}^1, and SM modes of β'-Ga$_2$S$_3$ disappear and more small peaks emerge between 180 and 300 cm^{-1}. Additionally, strong modes appear in the right and left side of A_{1g}^1 and A_{1g}^2 modes, respectively. The new Raman modes of φ-Ga$_2$S$_3$ are observed on downstroke between 9.9 and 1.0 GPa. At 0.5 GPa, a few broad peaks between 50 and 425 cm^{-1} emerge in the RS spectrum, thus suggesting a second PT (from φ-Ga$_2$S$_3$ to γ-Ga$_2$S$_3$) on decompression. The broad Raman peaks remain at ambient pressure, which points out the nonreversibility of the PTs of the original phase (α'-Ga$_2$S$_3$) at HP. All these changes are quite in agreement with earlier HP-RS measurements,[71] at least with the onset of the first PT on decompression. Regarding the second PT on decompression, Yang et al. observed the phase transition from φ-Ga$_2$S$_3$ to another phase (we will assume it is also γ-Ga$_2$S$_3$) below 3 GPa, but no Raman peaks both with He and without PTM, were reported for γ-Ga$_2$S$_3$.

As already commented, Yang et al. could not suggest any s.g. for both φ-Ga$_2$S$_3$ and γ-Ga$_2$S$_3$.[71] In this context, we have explored the literature on III−VI sesquichalcogenides to find potential candidates for φ-Ga$_2$S$_3$ and γ-Ga$_2$S$_3$. Both s.g. $R3m$ and R-$3m$ have been already observed in α- and β-In$_2$Se$_3$, respectively, and have been theoretically predicted in other III−VI sesquichalcogenides.[59,60,62,64] Moreover, the α-In$_2$Se$_3$-like structure in these compounds has been predicted to be dynamically stable at RC, unlike β-In$_2$Se$_3$-like structure.[59,62,64] On top of that, both are layered phases, the $R3m$ structure has 6 and 4-fold coordinated cations, while the R-$3m$ structure features only 6-fold coordinated cations. This decrease in the cation coordination from the former to the latter structure stands the $R3m$ phase as the candidate at LP on downstroke from the $R\bar{3}m$ phase. Consequently, in view of these antecedents, we have explored the α-In$_2$Se$_3$-like structure as a potential candidate for φ-Ga$_2$S$_3$.

According to group theory and considering the LO-TO splitting of the polar E modes in the noncentrosymmetric $R3m$ structure, there are 15 normal modes of vibration at Γ, whose mechanical decomposition is 3 acoustic $(A_1 + E_{TO} + E_{LO})$ modes and 12 optical $(4A_1(R, IR) + 4E_{TO}(R, IR) + 4E_{LO}(R, IR))$ modes. We have calculated the theoretical pressure dependence of the Raman frequencies in Ga$_2$S$_3$ with the $R3m$ structure and plotted them in Figure 3b together with those experimentally observed in φ-Ga$_2$S$_3$. In addition, we have tabulated the experimental pressure coefficients and zero-pressure frequencies of φ-Ga$_2$S$_3$ and those theoretically predicted for Ga$_2$S$_3$ with the $R3m$ structure in Table 1. The good agreement between the experimental and the calculated zero-pressure frequencies and pressure coefficients suggests that φ-Ga$_2$S$_3$ could have the $R3m$ structure. In this scenario, we have tentatively identified 8 of the 12 predicted Raman-active modes (see Figure 2b) and Figure 3b). At 1 GPa, they are the E^1 $(E_{TO}^1 + E_{LO}^1)$ mode at 47 cm^{-1}; the E_{TO}^2, E_{LO}^2, and A_1^1 modes between 135 and 175 cm^{-1}, the E_{TO}^3 mode at 260 cm^{-1}, and the E_{TO}^4, A_1^3, and E_{LO}^4 modes in the range between 275 and 350 cm^{-1}. We have not observed either the E_{LO}^3 mode (predicted around 282 cm^{-1}), the A_1^2 mode (predicted around 314 cm^{-1}), or the highest-frequency A_1^4 mode (predicted around 419 cm^{-1}). Curiously, this mode was observed by Yang
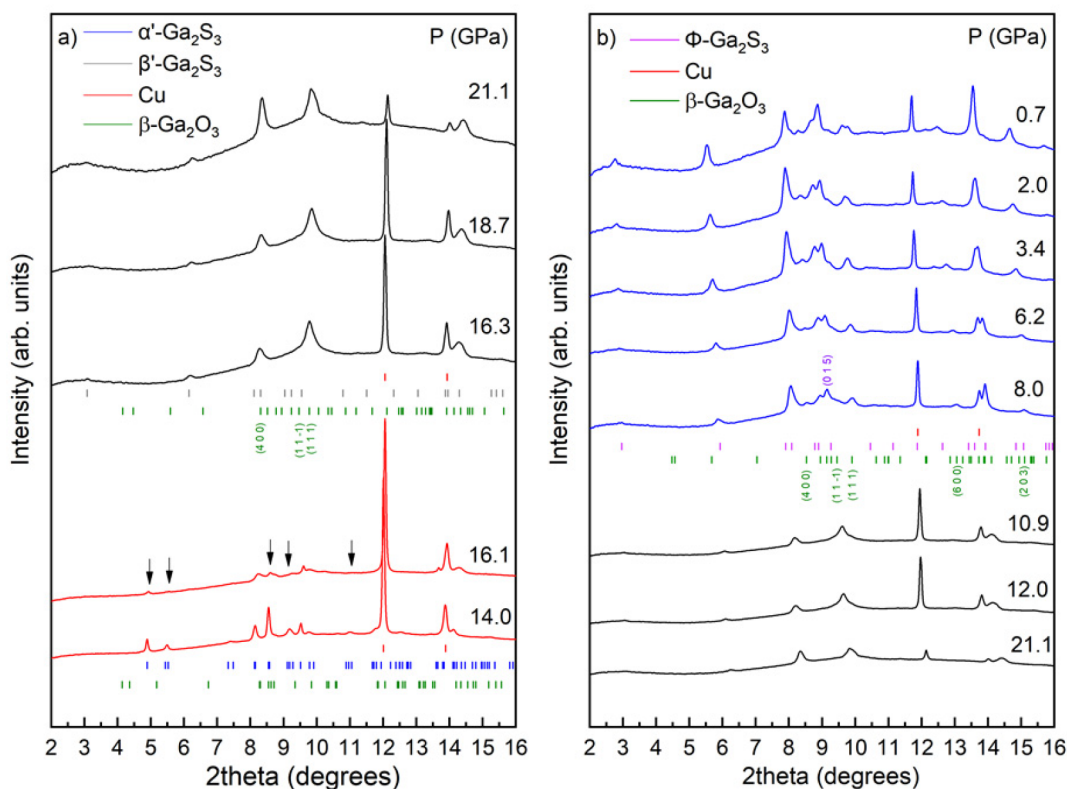
Figure 5. Selected normalized HP-XRD patterns of α'-Ga$_2$S$_3$ on the upstroke (a) and downstroke (b). Down arrows indicate the disappearance of several peaks of α'-Ga$_2$S$_3$ on the upstroke. XRD patterns in red, black, and blue colors correspond to α'-Ga$_2$S$_3$, β'-Ga$_2$S$_3$, and φ-Ga$_2$S$_3$, respectively. Blue, gray, purple, green, and red vertical ticks mark the α'-Ga$_2$S$_3$, β'-Ga$_2$S$_3$, φ-Ga$_2$S$_3$, β-Ga$_2$O$_3$, and copper Bragg reflections, respectively. The reader is referred to ref 70 for further information about the pressure dependence of the structure of α'-Ga$_2$S$_3$ and the presence of β-Ga$_2$O$_3$ identified as an impurity contained in the commercial sample. Several relevant reflections from β-Ga$_2$O$_3$ and φ-Ga$_2$S$_3$ are indicated.

et al. around 450 cm^{-1} (see Figures 2b and 3b of ref 71), which gives additional support to our assignment.

Further support to our assignment has been obtained from the comparison of the HP-RS spectra of φ-Ga$_2$S$_3$ at 7.6 GPa with that of α-In$_2$Se$_3$ at RC (Figure 4b). As observed, both RS spectra are rather similar and are dominated by a narrow and strong E^1 mode (this mode was not reported for α-In$_2$Se$_3$ in previous work[57] because of the edge filter cutoff in previous RS measurements). As observed, there is a nice agreement of experimental frequencies with theoretical frequencies (vertical ticks in Figure 4b). Note that vertical ticks of φ-Ga$_2$S$_3$ correspond to both calculated TO and LO counterparts of the E modes, while vertical ticks of α-In$_2$Se$_3$ correspond only to the theoretical A_1 and E_{TO} mode frequencies, since the LO counterpart of the polar E modes was not calculated in ref 57. Apart from the highest-intensity lowest-frequency E^1 mode, both RS spectra also show a rather strong A_1^1 mode and a complex band with at least the E_{TO}^4, A_1^3, and E_{LO}^4 modes. The main difference between both RS spectra is that E_{TO}^2 and E_{LO}^2 modes are observed at close frequencies in φ-Ga$_2$S$_3$, while they are quite apart in α-In$_2$Se$_3$.[57] Additionally, the highest-frequency A_1^4 mode found in α-In$_2$Se$_3$ and observed by Yang et al. in φ-Ga$_2$S$_3$[71] could not be seen in our HP-RS measurements, as already commented.

To verify if φ-Ga$_2$S$_3$ (R3m) is dynamically stable at RC, as suggested by refs 59 and 68, we have calculated the phonon dispersion curves of φ-Ga$_2$S$_3$ at 15 GPa (Figure S4c). It is observed that φ-Ga$_2$S$_3$ (R3m) is dynamically stable at that pressure. This result agrees with the experimental pressure value

of the β'-to-φ PT on decompression and the pressure range in which the φ-Ga$_2$S$_3$ is experimentally observed, according to this work and Yang et al.[71] In summary, we can conclude that our RS measurements and those of Yang et al. for φ-Ga$_2$S$_3$ are consistent with the experimental RS spectra of α-In$_2$Se$_3$ and consistent with the calculated Raman-active modes of the R3m phase in Ga$_2$S$_3$. Therefore, we consider that φ-Ga$_2$S$_3$ has the α-In$_2$Se$_3$-like structure. In the next section, we will confirm the α-In$_2$Se$_3$-like structure of φ-Ga$_2$S$_3$ with HP-XRD measurements and discuss the behavior of the structural properties of this new phase at HP.

Regarding the second phase observed on decompression, we only could measure two RS spectra, at 0.5 GPa and 1 atm (see bottom RS spectra in Figure 2b). Both RS spectra are dominated by broad bands, being the strongest one located around 250 cm^{-1}. The lack of narrow peaks suggest that this phase has a strong disorder corresponding either to amorphous α'-Ga$_2$S$_3$ nor to another disordered phase, as γ-Ga$_2$S$_3$. Since amorphous α'-Ga$_2$S$_3$ should show a RS spectrum that resembles the one-phonon density of states of crystalline α'-Ga$_2$S$_3$, we have compared the RS spectra of the recovered sample (γ-Ga$_2$S$_3$) near RC in Figure 2b with the one-phonon density of states of α'-Ga$_2$S$_3$ (see Figure S20 in ref 70) in order to verify whether the recovered sample could correspond to amorphous α'-Ga$_2$S$_3$. It can be observed that broad Raman bands in the RS spectrum of decompressed Ga$_2$S$_3$ are observed in the regions where bands of the one-phonon density of states are expected. However, we cannot explain the strongest Raman band near 250 cm^{-1} of decompressed Ga$_2$S$_3$ with the one-phonon density of states of
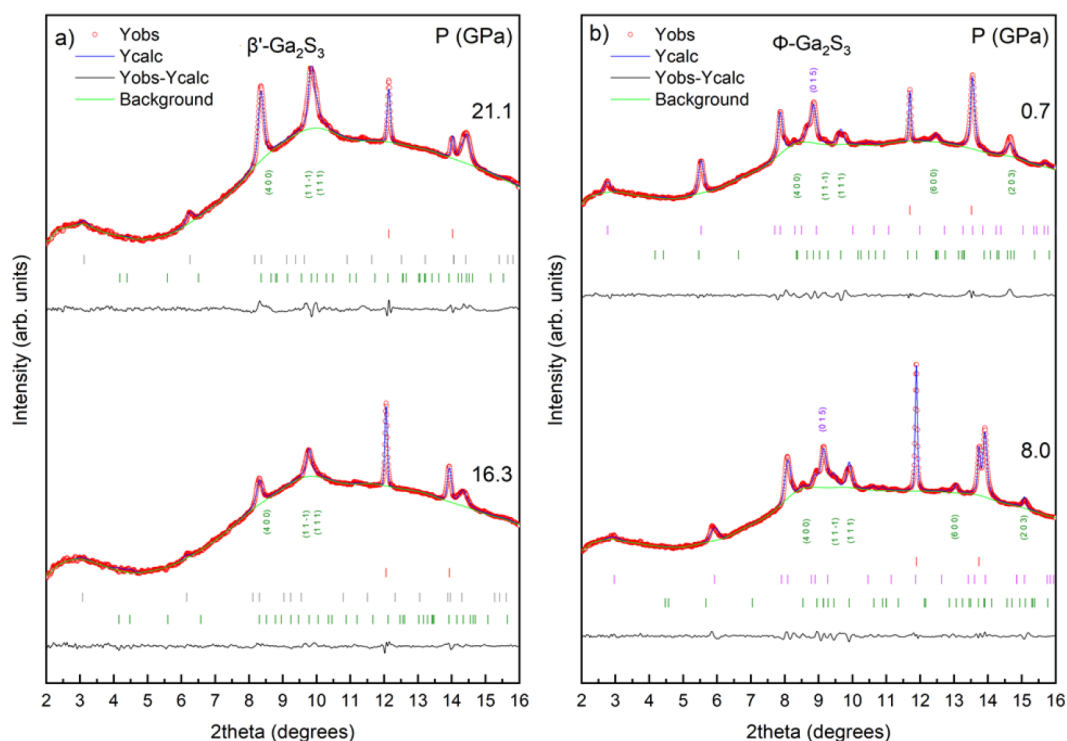
Figure 6. Selected normalized HP-XRD patterns of (a) β'-Ga$_2$S$_3$ on the upstroke and (b) φ-Ga$_2$S$_3$ on the downstroke. Gray, purple, green, and red vertical ticks mark the β'-Ga$_2$S$_3$, φ-Ga$_2$S$_3$, β-Ga$_2$O$_3$, and copper Bragg reflections. Several relevant reflections from β-Ga$_2$O$_3$ and φ-Ga$_2$S$_3$ are indicated.

crystalline α'-Ga$_2$S$_3$. Therefore, we conclude that it is not likely that the recovered sample corresponds to amorphous α'-Ga$_2$S$_3$.

On the other hand, it is well-known that γ-Ga$_2$S$_3$ is a HT phase with a DZ structure that is isostructural with α-Ga$_2$Se$_3$ and β-Ga$_2$Te$_3$[19,20,28−30] and that in the case of Ga$_2$Se$_3$ this DZ phase has also been observed at LT (α-Ga$_2$Se$_3$). Additionally, DZ structures have been obtained in several decompressed ternary AGa$_2$X$_4$ (A = Zn, Cd, Hg; X = S, Se) OVCs.[79,80] To investigate whether γ-Ga$_2$S$_3$ might have a DZ structure, we have plotted in Figure 4c the RS spectra of DZ γ- and α'-Ga$_2$S$_3$, DZ- and DC-CdGa$_2$S$_4$, DZ α-Ga$_2$Se$_3$, and DZ- and DC-CdGa$_2$Se$_4$. As can be observed, the RS spectrum of γ-Ga$_2$S$_3$ is very similar to that of DZ-CdGa$_2$S$_4$ with a broad and intense band near 250 cm^{-1}. Note also the similarities between the strongest Raman modes of ordered phases, like α'-Ga$_2$S$_3$[70] and DC-CdGa$_2$S$_4$[79] at 0.5 and 1.1 GPa, respectively, in Figure 4c. On the other hand, there is a notable difference between the RS spectra of ordered (red spectra) and disordered phases (green spectra) in all plotted compounds. The same comments done for the RS spectra of ordered and disordered phases of Ga$_2$S$_3$ are also valid for Ga$_2$Se$_3$ (see the comparison of DZ α-Ga$_2$Se$_3$,[74] DZ- and DC-CdGa$_2$Se$_4$[80] at 0.4, 1.0, and 1.2 GPa, respectively). In particular, the RS spectra of DZ α-Ga$_2$Se$_3$ is very similar to that of DZ-CdGa$_2$Se$_4$. Both compounds show a strong band located ∼150 cm^{-1} (Figure 4c). It must be stressed that the only difference between DZ-Ga$_2$X$_3$ and DZ-AGa$_2$X$_4$ compounds concerns the cation Wyckoff sites. In DZ-Ga$_2$X$_3$, the cation Wyckoff site is occupied by a mixture of Ga atoms and vacancies, while in DZ-AGa$_2$X$_4$ is occupied by a mixture of A and Ga atoms and vacancies.

The strongest peaks located at 250 and 150 cm^{-1} in DZ-CdGa$_2$S$_4$ and DZ-CdGa$_2$Se$_4$ (band 4 reported for both compounds from refs 79 and 80, respectively) were attributed to the highest-frequency and highest-intensity A^1 modes of DC-

CdGa$_2$S$_4$ and DC-CdGa$_2$Se$_4$, which represent the breathing mode; i.e., the vibration of anions against the vacancies. This mode is similar to the $A'(6)$ of the α'-Ga$_2$S$_3$, where S atoms vibrate toward the center of the channels. Instead, such strongest peaks in the RS spectra of these DZ phases correspond to an optical mode related to the vacancies and it has no counterpart in binary zincblende AX compounds (with no vacancies in the structure), as was discussed in refs 79 and 80. Therefore, on the light of the similitudes commented on here, we conclude that decompressed Ga$_2$S$_3$ likely has the same DZ structure as γ-Ga$_2$S$_3$. Future XRD measurements are needed to verify it; however, in the next section we will discuss the XRD patterns of the recovered samples reported by Yang et al.[71] that provide arguments to support the DZ structure of decompressed Ga$_2$S$_3$ at RC.

4.2. Structural Study under Compression and Decompression. *4.2.1. Compression.* Figure 5 shows normalized XRD patterns at selected pressures both on the upstroke and downstroke. As we have previously mentioned, in this work we focus on the pressure behavior of the HP phases of α'-Ga$_2$S$_3$, concretely, in β'-Ga$_2$S$_3$ and φ-Ga$_2$S$_3$ that are obtained under compression and decompression, respectively. Therefore, only a couple of XRD patterns of α'-Ga$_2$S$_3$ are shown at 14.0 and 16.1 GPa in Figure 5. We refer the reader to ref 70 for details about the structural pressure dependence of α'-Ga$_2$S$_3$ up to the PT to β'-Ga$_2$S$_3$. As stated in our previous work,[70] our HP-XRD patterns show Cu reflections that at certain pressures are even stronger than reflections of the HP phases observed both on compression and decompression; consequently, we have only been able to perform Le Bail refinements (see Figure 6).

Before analyzing the phases of Ga$_2$S$_3$, it must be mentioned that our HP-XRD measurements have detected the presence of an impurity in the commercial α'-Ga$_2$S$_3$ powders, as Lai et al. already did.[69] The presence of this impurity has not been

observed in our HP-RS measurements due to the small quantity in the original sample and the more local character of RS measurements than of XRD measurements. HT-RS spectra and Le Bail refinements of XRD patterns in ref 70 allowed us to identify this impurity as β-Ga_2O_3 (monoclinic, s.g. $C2/m$, No. 12). One can notice that, even though β-Ga_2O_3 is present in a small quantity (0.01% according to the product specifications from Alfa Aesar), the most intense peak at 9.8 degrees observed in our HP-XRD patterns belongs to this impurity. This intense peak is mainly composed of two reflections, the $(1\,1-1)$ and $(1\,1\,1)$ labeled in Figure 5a. In particular, the $(1\,1\,1)$ reflection shows the highest structure factor among all the reflections of β-Ga_2O_3, thus explaining the high intensity of this peak. Another relevant reflection to remark is the $(4\,0\,0)$, which makes the peak of β'-Ga_2S_3 located at about 8.5 degrees (Figure 5a and Figure 6b) broader. Therefore, vertical ticks as well as the such above-mentioned reflections indicating the presence of this impurity are provided in Figure 5 and Figure 6.

On the upstroke, we can observe remarkable changes in the XRD patterns (Figure 5a) between 16.1 and 16.3 GPa. Most of the α'-Ga_2S_3 peaks present at 16.1 GPa disappear at 16.3 GPa, and new ones emerge with smaller intensity than those of Cu (at about 12 and 14 degrees). The new peaks of the HP phase with relevant intensity are located at about 3.1, 6.2, 8.2, 9.8, and 14.3 degrees at 16.3 GPa (see Figure 5a and Figure 6a). Apart from the peaks of Cu and β-Ga_2O_3 (near 9.5 degrees), the new peaks of the XRD patterns from 16.3 to 21.1 GPa have been successfully refined via Le Bail method with the s.g. $R\overline{3}m$ of β'-Ga_2S_3 (Figure 5a and Figure 6a), thus supporting the results previously obtained by HP-RS measurements. Note that peaks at 8.2 and 14.3 degrees are overlapped reflections from both β'-Ga_2S_3 and β-Ga_2O_3. At 21.1 GPa, the maximum pressure achieved, the peaks of β'-Ga_2S_3 are clearly more intense than at 16.3 GPa (Figure 5a and Figure 6a) with the peak of β'-Ga_2S_3 located near 8.4 degrees being of similar intensity as that of β-Ga_2O_3.

It is important to stress that our HP-XRD measurements between 16.3 and 21.1 GPa at RT agree with earlier HP-XRD measurements at RT.[69] Lai et al. also used the same commercial α'-Ga_2S_3 powders and also reported the most intense peak around 0.4 Å^{-1} (corresponding to our 9.5 degrees) at 21 GPa at RT; i.e., prior to applying LH. However, since they could not identify the nature of the impurity, they could not refine the XRD pattern at RT with the β-In_2Se_3-like structure. Only the use of LH helped them to observe the β-In_2Se_3-like structure at 17.2 GPa in run-2, via improved crystallization, reducing possible internal, micro, and long-range internal stresses or anisotropic strains.[100] As a result, they improved the XRD signal of this structure, even making visible the two lowest reflections at about 0.14 and 0.26 Å^{-1} (in our HP-XRD patterns at about 3.1 and 6.2 degrees (Figure 5a and Figure 6a) and masking the signal of the impurity β-Ga_2O_3. All in all, our HP-XRD and HP-RS measurements, as well as previous HP-XRD and HP-RS measurements,[69] have clearly proved the feasibility of promoting the α'-to-β'-Ga_2S_3 PT at RT, with LH allowing one to improve the XRD signal of the β-In_2Se_3-like structure in Ga_2S_3 under compression.

4.2.2. Decompression. On the downstroke, XRD peaks from β'-Ga_2S_3 and the impurity, β-Ga_2O_3, increase their intensity down to 8 GPa (Figure 5b). On top of that, new peaks emerge from both phases, whose Miller indices (hkl) have been included. However, changes occur below 8 GPa. If we try to refine XRD patterns from 8 to 0.7 GPa via the Le Bail method

either with the s.g. R-$3m$ or with the $R3m$, we find a relatively good fit, but there is a discontinuity in the volume around 8 GPa. This means that, even though the impossibility of discerning the s.g. R-$3m$ and $R3m$ by powder XRD measurements, they can be distinguished by the volume discontinuity and the different pressure behavior below and above 8 GPa as we will discuss in the next subsection. For that reason, we have refined XRD patterns from 8 to 0.7 GPa with the s.g. $R3m$ structure of α-In_2Se_3 (see Figure 6b). Such refinements are consistent with the considerations made in section 4.1 regarding lattice dynamical experiments and calculations. The overall increase of the peak intensities, the emergence of new peaks, both from β-Ga_2O_3 and β'-Ga_2S_3, and thinner peaks from 8 GPa can be justified by the more hydrostatic conditions that allows the M–E, which does not guarantee such conditions above 10.5 GPa because of its glass transition.[101,102] The $(4\,0\,0)$, $(1\,1\,1)$, $(1\,1-1)$, $(6\,0\,0)$, and $(2\,0\,3)$ reflections of β-Ga_2O_3, marked in Figure 5b and Figure 6b, are similar to those found in the XRD measurements of α'-Ga_2S_3 in Figure 2 of ref 70 at about 8.3, 9.1, 9.6, 12.3, and 14.5 degrees, respectively, at 0.1 GPa.

At this point, we want to mention that a nice way to distinguish between centrosymmetric and noncentrosymmetric structures is by means of RS measurements, especially when analyzed together with lattice dynamics calculations.[103] Usually, noncentrosymmetric structures lead to a larger number of Raman-active modes than centrosymmetric structures, as has been shown for the $R3m$ and R-$3m$ phases of Ga_2S_3 in the previous section and in In_2Se_3.[57] Even for the identification of the α-In_2Se_3 ($R3m$) at RC, several works have carried out RS measurements to identify it from its centrosymmetric R-$3m$ and other phases.[57,104−107]

Further support to the existence of both $R\overline{3}m$ and $R3m$ phases in Ga_2S_3 is given by PBEsol total energy calculations of α'-Ga_2S_3 (Cc), φ-Ga_2S_3 ($R3m$), and β'-Ga_2S_3 (R-$3m$) in Figure S5a. It is shown that β'-Ga_2S_3 is energetically favorable above 9.5 GPa, while φ-Ga_2S_3 is energetically favorable between α'-Ga_2S_3 and β'-Ga_2S_3; i.e., between 5.2 and 9.5 GPa (Figure S5b). On top of that, our theoretical phonon dispersion curves of β'-Ga_2S_3 (R-$3m$) (Figure S4a) show that this phase is not dynamically stable for pressures below 17.6 GPa. On the contrary, φ-Ga_2S_3 ($R3m$) is energetically stable below 9.5 GPa and it is dynamic stable even at 15 GPa (Figure S4c) and, according to the previous theoretical works, is dynamically stable even at RC,[59,68] unlike β'-Ga_2S_3.[64] Consequently, we conclude that our combined HP-XRD and RS measurements supported by theoretical calculations have allowed us to confirm the R-$3m$ and $R3m$ nature of both β'-Ga_2S_3 and φ-Ga_2S_3, respectively.

Now the question is why the φ phase is not observed on the upstroke from the α' phase. The answer is that there is likely a kinetic energy barrier between the two phases that cannot be overcome without extra energy, and when this extra energy is obtained at higher pressure, there is another phase (in our case, β') that it is energetically more competitive. The existence of this kinetic energy barrier between the α' and φ phases on the upstroke is the minimum energy that we need to apply to the α' phase to move atoms in the direction of the φ phase, breaking bonds of the α' phase to favor the formation of new bonds in the φ phase. This kinetic energy barrier is the same that avoids the transition from the φ phase to the α' phase on the downstroke, giving support to the transition from the φ phase to the DZ phase on the downstroke. Note that we have not included the DZ phase in Figure S5 because of the fractional occupation of the cation positions in this phase makes it difficult to simulate

this structure. However, we consider that the DZ phase must be a metastable structure competitive in energy with the α' phase since this phase has been also observed in Ga_2Se_3 and Ga_2Te_3 at RC.[19,20,28−30]

Regarding the second PT on the downstroke, we have tentatively attributed it to the DZ structure of γ-Ga_2S_3 by considering the similarity of our RS measurements and those of DZ-$CdGa_2S_4$ and also the similarity of the RS spectra of DZ γ-Ga_2Se_3 and DZ-$CdGa_2S_4$ (Figure 4c). As it was previously commented, we could not measure XRD patterns below 0.7 GPa; therefore, we do not have XRD data to identify the structure of γ-Ga_2S_3. However, we want to comment on the XRD results obtained by Yang et al. on α'-Ga_2S_3 since they showed XRD patterns of the recovered samples (Figure 8 of ref 71). Unfortunately, Yang et al. did not provide any information about the PTM used in one of their runs, the type of gasket used, and the X-ray wavelength employed for the XRD measurements, so we cannot discuss their patterns in quantitative terms. In qualitative terms, however, we can conclude that Figure 8 of ref 71 undoubtedly shows that the recovered XRD pattern does not match with the original α'-Ga_2S_3. Moreover, we can tentatively identify the peaks located at around 0.26 and 0.27 Å^{-1} with the $(1\,1\,1)$ and $(2\,0\,0)$ reflections of the DZ-type structure, as can be seen in the recovered DZ-$CdGa_2Se_4$ in ref 108. The rest of the peaks do not match with other reflections of the DZ structure, and they could be related with highly-intense β-Ga_2O_3 or PTM reflections instead.

Additional support to the observation of the DZ phase in decompressed Ga_2S_3 comes from the fact that both β'-Ga_2S_3 and φ-Ga_2S_3 show vacancies in the structure, so an order−disorder PT can occur on the downstroke. In this context, we must note that β'-Ga_2S_3 is a distorted rocksalt phase with a 6-fold coordinated cation that has a plane of vacancies forming the interlayer space.[99,109] Similarly, φ-Ga_2S_3 has cations with 6-fold and 4-fold coordination and also has the same plane of vacancies at the interlayer space. Therefore, a PT to the DZ phase on downstroke in α'-Ga_2S_3 is highly possible in its way to attain a 4-fold cation coordination at RC if no thermal energy is added to the system. Note that the original Cc structure of α'-Ga_2S_3 is an ordered phase with vacancies located on well-defined channels that could be difficult to obtain at RC on the downstroke without additional thermal energy. This can be seen as the presence of an energy barrier between the α' and φ phases already discussed. In summary, we conclude that the recovered phase on the downstroke is likely γ-Ga_2S_3 with a DZ structure; however, further XRD measurements should be carried out to verify the DZ nature of the recovered phase from the structural point of view.

4.2.3. Pressure Dependence of Lattice Parameters and Volume of β'- and φ-Ga_2S_3.

Let us now analyze the pressure dependence of the structural parameters of both β'-Ga_2S_3 and φ-Ga_2S_3. Figure 7a shows the experimental and theoretical PBEsol and PBE-D3 pressure dependence of the lattice parameters of β'-Ga_2S_3 and φ-Ga_2S_3. Additionally, experimental and theoretical LDA data sets of β'-Ga_2S_3 from Lai et al.[69] are included. In regards to β'-Ga_2S_3, our experimental a and c values are slightly larger than those reported by Lai et al. This difference likely stems from the different PTM used or to the LH employed by Lai et al. to assist the α'-to-β' PT. Theoretical PBE-D3 calculations predict c values closer to those experimental ones than PBEsol and LDA calculations. On the other hand, the three theoretical calculations predict similar values for the lattice parameter a, with a tendency of LDA > PBE-D3 > PBEsol.
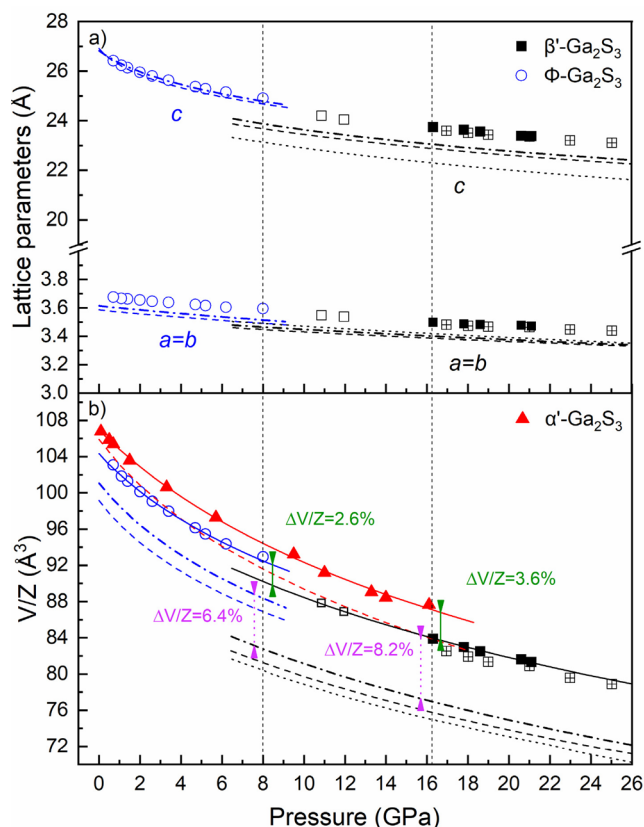

Figure 7. Pressure dependence of (a) lattice parameters and (b) volume per formula unit, V/Z (b), in α'-Ga_2S_3, β'-Ga_2S_3, and φ-Ga_2S_3. Full and open symbols represent experimental data under compression and decompression, respectively. Theoretical PBEsol (dashed lines) and PBE-D3 (dashed dotted lines) pressure dependence of lattice parameters in β' and φ phases is plotted in part a. Experimental (solid lines) and theoretical (dashed lines) BM3-EoS for the α', β', and φ phases are shown in part b. Theoretical PBEsol and experimental $\Delta V/Z$ observed in the α'-β' and β'-φ phase transitions are indicated in dark green and magenta, respectively. For the sake of comparison, the experimental (black squared plus symbols) and theoretical (LDA, dot lines) pressure dependence of the lattice parameters of the β' phase from ref 69 are included in panel a, while theoretical (LDA, dotted lines) BM3-EoS from the β' phase from ref 69 is included in panel b.

Concerning φ-Ga_2S_3, our theoretical PBE-D3 calculations predict the experimental c values perfectly and also the a values are better predicted with PBE-D3 calculations than with PBEsol calculations. One can notice that the experimental and theoretical a values of β'-Ga_2S_3 and φ-Ga_2S_3 have an almost linear pressure dependence along the whole range of pressures. On the other hand, the experimental c values of both phases show a more nonlinear pressure dependence because both β'-Ga_2S_3 and φ-Ga_2S_3 are layered phases whose interlayer space have a big compression at LP and a much smaller compression at HP as a consequence of the hardening of the interlayer vdW bonds at HP.

Table 2 gathers the zero-pressure axial compressibilities, defined as $\kappa_x = -\frac{1}{x}\frac{\partial x}{\partial P}$, of both the a and c axes for β'-Ga_2S_3 and φ-Ga_2S_3. As expected from any 2D material, the c axis (OP direction) is more compressible than the a (and b) axis (IP directions). For β'-Ga_2S_3, our experimental values for K_a are quite close to theoretical PBEsol and PBE-D3 calculations and much smaller than the experimental and theoretical LDA values of Lai et al.[69] In contrast, our experimental K_c value is similar to

Table 2. Experimental (exp.) and Theoretical PBEsol and PBE-D3 (th.) Zero-Pressure Axial Compressibilities (K_a and K_c, in 10^{-3} GPa^{-1}), Zero-Pressure Unit-Cell Volume (V_0, in Å^3), Bulk Modulus (B_0, in GPa), and Bulk Modulus First Pressure Derivative (B_0') for β'- and φ-Ga$_2$S$_3$[a]

		K_a	K_c	V_0	B_0	B_0'
β'-Ga$_2$S$_3$	exp.[b]	2.5(1)	8.0(1)	297(1)	66(2)	5.4(2)
				295(1)	74(3)	4 (fixed)
	PBEsol[b]	3.5(1)	9.5(1)	269(1)	64(1)	4.9(2)
				266(1)	76(1)	4 (fixed)
	PBE-D3[b]	3.3(1)	14.6(1)	276(1)	59(1)	4.9
				272(1)	71(1)	4 (fixed)
	exp.[c]	7.2(1)	18.2(1)	270(1)	91(3)	4 (fixed)
	LDA[c]	11.3(1)	31.1(1)	264(1)	75(2)	3.9(3)
				264(3)	74(1)	4 (fixed)
β-In$_2$Se$_3$	exp.[d]	1.6(1)	6.8(1)	375(2)	60(6)	4 (fixed)
	exp.[e]			370	66	4 (fixed)
	PBE[d]	3.2(1)	5.1(1)	382(1)	50(1)	4.7(2)
				375(1)	61(1)	4 (fixed)
φ-Ga$_2$S$_3$	exp.[b]	3.9(1)	12.0(1)	313(1)	41(2)	8.2(1)
				311(1)	53(2)	4 (fixed)
	PBEsol[b]	3.9(1)	16.0(1)	297(1)	33(1)	9.9(1)
				294(1)	51(1)	4 (fixed)
	PBE-D3[b]	4.2(1)	23.1(1)	303(1)	36(1)	8.1(1)
				302(1)	46(1)	4 (fixed)
α-In$_2$Se$_3$	exp.[d]			401(1)	40(2)	4 (fixed)
	exp.[e]			407.9	31	4 (fixed)
	PBE[d]	6.1(1)	20(1)	436(1)	23(1)	3.3(1)
				434(1)	26(2)	4 (fixed)

[a]Results of β'-Ga$_2$S$_3$ and β- and α-In$_2$Se$_3$ from previous HP works have been added for comparison. [b]Present work. [c]Reference 69. [d]Reference 57. [e]Reference 58.

the theoretical PBEsol one, smaller (almost half) than that predicted by PBE-D3 calculations, and much smaller than the experimental and theoretical LDA values of Lai et al. Taking into account all experimental and theoretical data available (including extrapolated theoretical LDA and experimental data sets reported by Lai et al.[69] and included in Table 2), we can see that both the values of K_a and K_c follow the same tendency: LDA[69] > experimental[69] > PBE-D3 > PBEsol > experimental (ours). In fact, our experimental and theoretical K_a and K_c values are much smaller (around three times) than those obtained by Lai et al. and also much smaller than those from their theoretical LDA calculations. On the other hand, the experimental values of K_a and K_c for β-In$_2$Se$_3$ from ref 57 (see Table 2) are similar although slightly smaller than those obtained by us for β'-Ga$_2$S$_3$. This result shows the consistency of our values for β'-Ga$_2$S$_3$ and indicate that the $R\bar{3}m$ phase in In$_2$Se$_3$ exhibits a larger compressibility than in Ga$_2$S$_3$.

Regarding φ-Ga$_2$S$_3$, the experimental and theoretical PBEsol K_a and K_c values are in good agreement. However, theoretical PBE-D3 calculations predict a K_c value higher than those of theoretical PBEsol calculations and experiments. Comparison of experimental K_a and K_c values of φ-Ga$_2$S$_3$ with experimental values for α-In$_2$Se$_3$ is not possible because only a few XRD measurements were obtained at a few pressures in ref 57, and it is not possible to obtain such parameters. However, theoretical PBE calculations for α-In$_2$Se$_3$ from ref 57 yields values of K_a and K_c of similar magnitude as those calculated in φ-Ga$_2$S$_3$ (see Table 2). Additionally, theoretical PBE calculations for α-In$_2$Se$_3$ also yield K_a and K_c values that are higher than those for β-In$_2$Se$_3$. This is also found in Ga$_2$S$_3$ that shows K_a and K_c values in φ-Ga$_2$S$_3$ that are 60% larger than those in β'-Ga$_2$S$_3$. These results agree with what it is expected for a $R3m$ phase, with 6- and 4-fold

coordinated cations, in contrast with the $R\bar{3}m$ phase, with only 6-fold coordinated cations. Therefore, the existence of the β'-to-φ PT on the downstroke is consistent with the large differences found between the zero-pressure axial compressibilities of both phases, both experimentally and theoretically.

As already mentioned, strong evidence of the existence of the β'-to-φ PT on the downstroke also arises from the relative volume change at the PT pressure. Figure 7b shows the experimental and theoretical PBEsol pressure dependence of the unit-cell volume per formula unit, V/Z, in α'-Ga$_2$S$_3$, β'-Ga$_2$S$_3$, and φ-Ga$_2$S$_3$. In addition, the theoretical PBE-D3 pressure dependence of V/Z is also included for β'- and φ-Ga$_2$S$_3$. All data in Figure 7b have been fitted to a third-order Birch−Murnaghan equation of state (BM3-EoS), whose values of zero-pressure volume, V_0, bulk modulus, B_0, and its pressure derivative, B_0', are summarized in Table 2. Also the experimental pressure dependence of V/Z, the BM2-EoS, and the theoretical LDA BM2-EoS and BM3-EoS obtained for β'-Ga$_2$S$_3$ by Lai et al.[69] are included in both Figure 7b and Table 2 for comparison. Concerning the α'-to-β' PT, we have observed a 3.6% decrease of the experimental relative change of the unit-cell volume per formula unit, $\Delta V/Z$. Our PBE-D3 (PBEsol) calculations predict a $\Delta V/Z$ decrease of 8.2% (9.8%); i.e., more than 2 times the experimental one. These results compare with the experimental and theoretical LDA $\Delta V/Z$ around 11% reported by Lai et al.[69] The experimental $\Delta V/Z$ reported by Lai et al. is 3 times larger than ours, which can be explained not only for a PTM (LiF plates) that is less hydrostatic than ours (M−E) but also because of the use of LH. On the other hand, their theoretical LDA $\Delta V/Z$ is 34% larger than ours. That makes sense if we consider that the theoretical LDA calculations for β'-Ga$_2$S$_3$ predict a much smaller volume than our calculations for β'-Ga$_2$S$_3$. On the
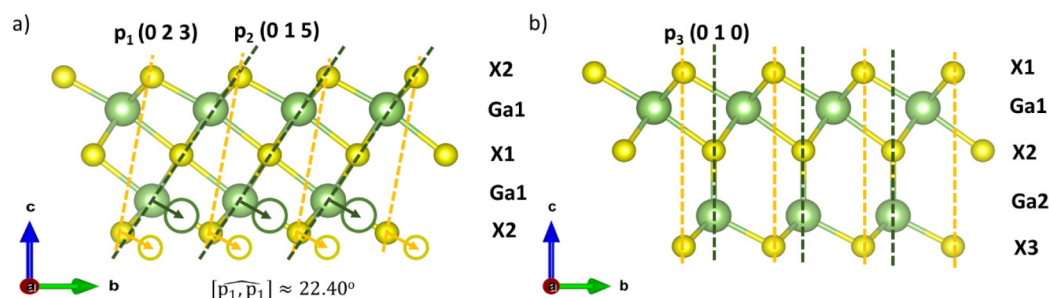
Figure 8. Side view parallel to the a axis of (a) paraelectric, centrosymmetric β'-Ga$_2$X$_3$ and (b) ferroelectric, noncentrosymmetric φ-Ga$_2$X$_3$ phases. (0 2 3) and (0 1 5) planes based on $X2-X2$ and Ga1$-X1$ atoms, respectively, of β'-Ga$_2$X$_3$ phases transform into (0 1 0) planes in φ-Ga$_2$X$_3$ phases. (0 2 3) and (0 1 5) planes that are secant, with an angle of 22.40°, become parallel (0 1 0) planes.

downstroke, the β'-to-φ PT shows an experimental $\Delta V/Z$ increase of 2.6% that compares with the theoretical PBE-D3 (PBEsol) values of 6.4% (7.1%). Therefore, our calculations predict $\Delta V/Z$ for both α'-to-β' and β'-to-φ PTs that are at least 2 times larger than experimentally measured.

Let us analyze now the pressure behavior of the experimental and theoretical unit-cell volumes of β'-Ga$_2$S$_3$ and φ-Ga$_2$S$_3$. As already commented, Table 2 summarizes the values of V_0, B_0, and B_0' of our experimental and theoretical (PBEsol and PBE-D3) data for β'-Ga$_2$S$_3$ and φ-Ga$_2$S$_3$, as obtained from fits to a BM3-EoS or to a BM2-EoS (B_0' fixed to 4). Also, experimental and theoretical LDA data for β'-Ga$_2$S$_3$ from ref 69 are analyzed. It can be observed that for β'-Ga$_2$S$_3$ there is a good agreement between our experimental values for B_0 and B_0' and theoretical (LDA, PBEsol, and PBE-D3) values. This means that our experimental pressure behavior of the unit-cell volume is well accounted for by calculations, despite the disagreement in the absolute value of V_0 (only theoretical PBE-D3 calculations yield a V_0 closer to the experimental value). It is well-known that LDA and PBEsol calculations usually yield understimated V_0 values for layered vdW materials and much better agreement is obtained with PBE-D3 calculations that include vdW interactions. In this context, we must stress that experimental V_0 for β'-Ga$_2$S$_3$ is difficult to obtain since experimental values are extrapolated from above 8 to 0 GPa always with considerable uncertainty. On the other hand, the experimental B_0 of Lai et al. is considerably larger than calculations, thus showing a larger incompressibility of β'-Ga$_2$S$_3$ compared to our experiments. This result can be understood if we consider that Lai et al. made a fit over a very small range of pressures (17−25 GPa)) while we have used a much larger range of pressures for the fit (11−23 GPa), in addition to their not so hydrostatic PTM (LiF plates) and the LH employed. Finally, we have to note that the experimental and theoretical B_0 values obtained in this work for the R-3m phase of Ga$_2$S$_3$ are of the same order as those obtained for the R-3m phase of In$_2$Se$_3$,[57] which gives us confidence about our present results.

Concerning φ-Ga$_2$S$_3$, there is a nice agreement between the experimental and theoretical (PBEsol and PBE-D3) values of V_0, B_0, and B_0'. It can be observed that φ-Ga$_2$S$_3$ is more compressible than β'-Ga$_2$S$_3$, as expected for the lower atomic coordination of the former phase. Additionally, the experimental and theoretical B_0 values obtained in this work for the R3m phase of Ga$_2$S$_3$ are of the same order as those obtained for the R3m phase of In$_2$Se$_3$,[57] which again gives us confidence about our present results.

In summary, we can conclude that the analysis of the structural parameters of φ-Ga$_2$S$_3$ and β'-Ga$_2$S$_3$ has allowed us to

clearly distinguish between the respective R3m and R-3m phases. Note that the pressure dependence of their lattice parameters a and c and volume, more specifically, the zero-pressure axial compressibilities (K_a and K_c) as well as the bulk modulus, B_0, and its pressure derivative, B_0', of the two phases are clearly different, as it is already confirmed by our theoretical calculations. Moreover, RS scattering measurements are clearly different in both phases and the observed Raman-active modes in both phases are consistent with the R3m and R-3m phases of φ-Ga$_2$S$_3$ and β'-Ga$_2$S$_3$, respectively. Additionally, HP electrical conductivity measurements carried out by Yang et al.[71] show relevant changes below 9 GPa, which is another significant indicator of the β'-to-φ PT.

4.3. Mechanism of the $R\bar{3}m$-to-$R3m$ Phase Transition in B_2X_3 (B = Ga, In; X = S, Se, Te) Compounds. Now we are going to describe the PT mechanism between the $R\bar{3}m$ and $R3m$ structures in B_2X_3 (B = Ga, In; X = S, Se, Te) compounds. For that purpose, we are going to focus on the R-3m-to-R3m PT in Ga$_2$S$_3$ (see Figure 8). On one hand, the centrosymmetric $R\bar{3}m$ tetradymite-like structure of β'-Ga$_2$S$_3$ is a layered structure composed of quintuple layers and presents a 3-fold rotoinversion axis with only one independent Ga atom, Ga1, and two independent S atoms, S1 (internal anion of the layer) and S2 (external anion of the layer). In this way, the quintuple layers stacked along the c axis are formed by alternate S2−Ga1−S1−Ga1−S2 atoms (Figure 8a). In this structure, Ga1 cation is 6-fold coordinated, the internal S1 anion is also 6-fold coordinated, and the external S2 anion is 3-fold coordinated. On the other hand, the noncentrosymmetric $R3m$ structure of φ-Ga$_2$S$_3$ is also a layered structure composed of quintuple layers and presents a 3-fold axis with two independent Ga atoms, Ga1 and Ga2, and three independent S atoms, S1, S2, and S3. In this way, the quintuple layers along the c axis are formed by S1−Ga1−S2−Ga2−S3 atoms. In this structure, Ga1 is 6-fold coordinated, Ga2 is 4-fold coordinated, the internal S2 anion is 4-fold coordinated, and the external S1 and S3 anions are 3-fold coordinated (Figure 8b).

To describe the mechanism of the R-3m-to-R3m PT in Figure 8, we draw lines along the (0 2 3) planes (planes p$_1$) in the R-3m structure that contain S2 atoms from the top and the bottom of the layers (Figure 8a). We also draw lines along the (0 1 5) planes (planes p$_2$) that contain the sequence S2−Ga1−S1−Ga1−S2. These two families of planes intersect at the S2 atoms and form an angle of ∼22.4 deg above 9 GPa. At the PT below 9 GPa, there is a gliding of the Ga1 and S2 atoms in these two planes along the (1 1−1) direction of the $R\bar{3}m$ phase, as it is illustrated in Figure 8a. This gliding can be seen as the rotation of the p$_1$ and p$_2$ planes in β'-Ga$_2$S$_3$ (Figure 8a) in the anticlockwise

direction, yielding parallel (0 1 0) planes (plane p$_3$) in φ-Ga$_2$S$_3$ (Figure 8b). This gliding leads to the disappearance of the 3-fold rotoinversion axis of the $R\bar{3}m$ phase giving rise a 3-fold axis and to two Ga and three S atom types in the $R3m$ phase (Figure 8b). The gliding also leads to the breaking of the half of Ga1−S1 bonds in β'-Ga$_2$S$_3$, yielding the change from 6-to-4 fold coordination of the Ga atoms that are now Ga2 atoms in φ-Ga$_2$S$_3$ (Figure 8b). As a result of this gliding, there is a jump in the lattice parameter c, without a jump in the lattice parameter a (Figure 7a). In this context, we must note that the jump in the c value occurs despite bonds in the tetrahedra being shorter than the octahedra because one of the Ga−S bonds in φ-Ga$_2$S$_3$ is parallel to the c axis.

At this point, we want to comment on the reverse PT; i.e., from the $R3m$ to the $R\text{-}3m$ phase on increasing pressure. This HP-PT would be driven by a gliding of Ga2 and S3 atoms in the $R3m$ phase along the (111) direction of the hexagonal lattice of the $R3m$ structure. In this way, both 4-fold-coordinated cations and anions become 6-fold-coordinated in the $R\text{-}3m$ phase. However, this simple step seems not to occur in In$_2$Se$_3$ because of the appearance of an intermediate β'(C2/m) phase under increasing pressure.[57]

Now we want to comment on the role of temperature as a driving force to promote the $R3m$-to-$R\text{-}3m$ PT (or vice versa). This HT-PT was studied in B_2X_3 compounds by means of molecular dynamics calculations (Figure 4 and Figure S4 in ref 62). Their results agree totally with our PT mechanism proposed on decompression. The $R3m$-to-$R\text{-}3m$ HT-PT is driven by the gliding of $B2$ and $X3$ layers in $R3m$, becoming $B1$ and $X2$ layers in $R\text{-}3m$. This is the reverse direction that we propose in Figure 8 for the $R\text{-}3m$-to-$R3m$ PT on decompression. Additionally, the molecular dynamics simulations corroborated the mechanism of the $R3m$-to-$R\text{-}3m$ PT at HT experimentally observed in α-In$_2$Se$_3$.[55,56,110] In a more recent work,[64] the feasibility of $R3m$-to-$R\text{-}3m$ PT at HT was evaluated again via molecular dynamics calculations. For the opposite PT ($R\text{-}3m$-to-$R3m$), they revealed a Mexican-hat potential energy surface (a general feature of these B_2X_3 compounds), which acts as an entropy barrier that hampers such PT on decreasing temperature. To overcome such entropy barrier, the application of an OP electric field was proposed. However, upon decompression we have observed in our results, in agreement with those reported by Yang et al.,[71] that β'-Ga$_2$S$_3$ turns into φ-Ga$_2$S$_3$ by just decreasing the pressure, without the need to apply external fields or LH. We think that molecular dynamics calculations are needed to study the $R3m$-to-$R\text{-}3m$ HP-PT in all B_2X_3 sesquichalcogenides, which complement the already performed molecular dynamics simulations of this PT at HT.[62,64] Those calculations will allow to verify the barriers between these phases at different pressures.

4.4. Relation between the HP Phases of Ga$_2X_3$ (X = S, Se, Te) and AGa$_2X_4$ (X = S, Se) Compounds.

It has been previously commented that β'-Ga$_2$Te$_3$ ($R\bar{3}m$) was observed above 5 GPa from β-Ga$_2$Te$_3$ (DZ).[75] However, there is still no experimental evidence of β'-Ga$_2$Se$_3$ ($R\text{-}3m$) neither at RC nor at HP. At this point, we have wondered if the $R3m$ and the $R\text{-}3m$ phases are energetically competitive in Ga$_2$Se$_3$ and Ga$_2$Te$_3$. To answer this question, we have performed DFT PBEsol calculations of several phases in both compounds (see Figures S6 and S7). We have named β' and φ the corresponding $R\bar{3}m$ and $R3m$ phases in Ga$_2$Se$_3$ and Ga$_2$Te$_3$. As already commented on, we have not included either the DZ or DR phases of both compounds because the fractional occupation of cation

positions in both phases makes it difficult to simulate these structures.

Figure S6a provides evidence that only mono-β-Ga$_2$Se$_3$ and β'-Ga$_2$Se$_3$ are energetically more favorable than ortho-β-Ga$_2$Se$_3$ and φ-Ga$_2$Se$_3$. Taking mono-β-Ga$_2$Se$_3$ and ortho-β-Ga$_2$Se$_3$ as references, β'-Ga$_2$Se$_3$ ($R\bar{3}m$) is predicted to occur above 6.8 (Figure S6b) and 5.8 GPa (Figure S6c), respectively, while φ-Ga$_2$Se$_3$ ($R3m$) is not expected to occur in this sesquichalcogenide. In this context, it is known that DZ α-Ga$_2$Se$_3$ and mono-β-Ga$_2$Se$_3$ undergo a PT to DR-Ga$_2$Se$_3$ above 14 GPa,[72−74] with the DZ-to-DR PT reversible. Concerning the ortho-β-Ga$_2$Se$_3$, there are no HP studies; therefore, further HP works are required to unveil the possibility that the $R\text{-}3m$ phase could be obtained at HP in Ga$_2$Se$_3$.

Regarding Ga$_2$Te$_3$, Figure S7a shows that φ-Ga$_2$Te$_3$ ($R3m$) is energetically favorable between mono-α-Ga$_2$Te$_3$ and ortho-α-Ga$_2$Te$_3$ and β'-Ga$_2$Te$_3$ ($R\text{-}3m$), as it occurs in Ga$_2$S$_3$. Again, taking mono-α-Ga$_2$Te$_3$ and ortho-α-Ga$_2$Te$_3$ as references, φ-Ga$_2$Te$_3$ is predicted between 11.2 and 11.6 GPa and between 7.2 and 11.6 GPa (Figure S7b and Figure S7c), respectively, while β'-Ga$_2$Te$_3$ is predicted above 11.6 GPa. At HP, only an α-Ga$_2$Te$_3$ with a DZ structure has been studied and β'-Ga$_2$Te$_3$ has been obtained above 5 GPa, thus giving support to our calculations.[75] Moreover, HP-electrical measurements have suggested the reversibility of the α-to-β'-Ga$_2$Te$_3$ HP-PT.[111] Therefore, future HP works devoted to both mono-α-Ga$_2$Te$_3$ and ortho-α-Ga$_2$Te$_3$ are needed to explore whether both β' ($R\text{-}3m$) and φ ($R3m$) phases can be attained at HP. If such a β'-to-φ PT is observed in Ga$_2$Te$_3$, the PT mechanism could be the mechanism explained in the previous section.

The theoretical calculations mentioned in the previous paragraphs and the experiments performed in the three Ga$_2X_3$ sesquichalcogenides mentioned in the Introduction section show that phases at RC, at HT, and at HP are related in these compounds. In particular, they exhibit DZ phases (γ-Ga$_2$S$_3$, α-Ga$_2$Se$_3$, and β-Ga$_2$Te$_3$) or a wurtzite-like superstructure (monoclinic α'-Ga$_2$S$_3$, β-Ga$_2$Se$_3$, α-Ga$_2$Te$_3$, and orthorhombic β-Ga$_2$Se$_3$ and α-Ga$_2$Te$_3$) at RC or at HT.[23] The difference between them is that the former are disordered phases featuring cation-vacancy mixing at cation positions and the latter exhibit ordered vacancies forming channels. Additionally, these compounds show either the DR (in Ga$_2$Se$_3$) or $R\text{-}3m$ (in Ga$_2$S$_3$ and Ga$_2$Te$_3$) phases at HP (being the $R3m$ phase, observed in this work for the first time in Ga$_2$S$_3$, also energetically competitive in Ga$_2$Te$_3$). Considering that the $R\bar{3}m$ phase is a distortion of the rocksalt structure, we can establish that all Ga$_2X_3$ sesquichalcogenides share a common NaCl-like phase at HP. Both DR and $R\text{-}3m$ phases differ in the way that vacancies are located. In the DR phase, the 6-fold coordinated cations are mixed with vacancies at cations sites. In contrast, in the β' phase, the 6-fold coordinated cations are ordered and vacancies form planes (interlayer space). Since both Ga$_2$S$_3$ and Ga$_2$Te$_3$ show the $R\text{-}3m$ phase at HP, we can speculate that the observation of either the DR or $R\bar{3}m$ phases is not related to the anion size but perhaps to the crystalline structure of the original phase being compressed. In this context, more works of the different polymorphs of these chalcogenides at HP are needed to verify this hypothesis.

What happens when the pressure is totally released can be considered another common point of Ga$_2X_3$ sesquichalcogenides. These compounds usually exhibit a tetrahedral coordination in the original structure at RC, and this coordination is again recovered on the downstroke despite that the PTs at HP could
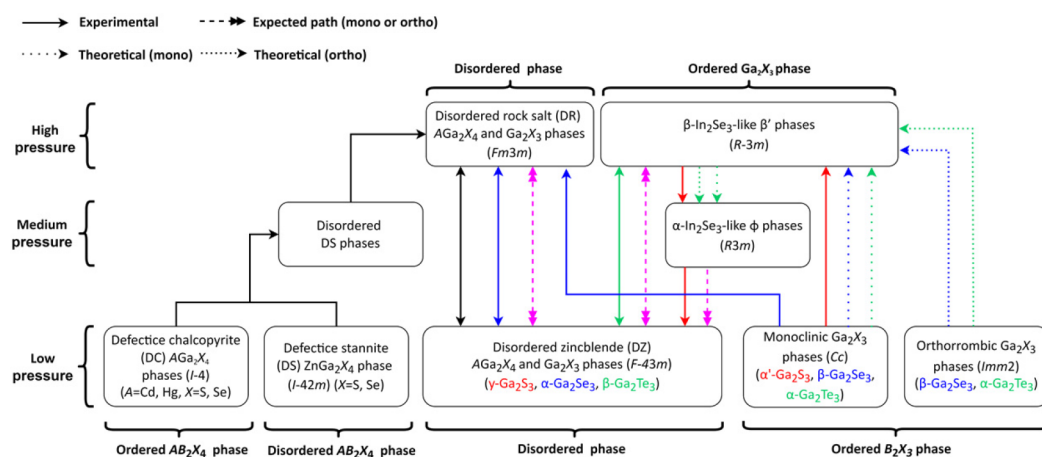
Figure 9. Schematic representation of the behavior of Ga_2X_3 (X = S, Se, Te) and AGa_2X_4 (X = S, Se) chalcogenides at high pressure. Black solid arrows are for those phase transitions related to the AGa_2X_4 compounds experimentally observed. Red, blue, and green solid arrows show the same for Ga_2S_3, Ga_2Se_3, and Ga_2Te_3, respectively. Blue and green dot arrows refer to the theoretical predicted phase transitions for Ga_2Se_3 and Ga_2Te_3, starting from their monoclinic (Cc) phases. The same applies for the blue and green short dot arrows but from their orthorhombic ($Imm2$) phases. Pink dashed double arrows indicate that phase transitions are expected from both the monoclinic and orthorhombic phases, from Ga_2S_3, Ga_2Se_3, and Ga_2Te_3.

not be reversible; i.e., do not return to the original phase. In this context, it is expected that all Ga_2X_3 phases at LP tend to exhibit the DZ phase with 4-fold coordinated cations mixed with vacancies in the same crystallographic site.

It must be noted that the DZ-to-DR HP-PT is usually reversible since both the initial and final structures are already fully disordered. This has been observed in DZ α-Ga_2Se_3 that transforms into the DR phase (Fm-$3m$) on compression.[72,74] Curiously, DZ α-Ga_2Te_3 turns into β'-Ga_2Te_3 (R-$3m$) on compression,[75] and it has been suggested on the basis of resistivity studies at HP that this PT is reversible.[111] In this context, further HP experiments must be conducted in these compounds and especially in DZ-Ga_2S_3 to see if it will undergo a PT to β'-Ga_2S_3 or to the DR phase on compression. We initially expect that DZ-Ga_2S_3 undergoes a reversible PT to the DR phase at HP, as it occurs in Ga_2Se_3[72,74] and also in $CdGa_2S_4$[79] and $CdGa_2Se_4$.[80]

Now, we will review the phases of AGa_2X_4 (X = S, Se) OVCs at LP and HP to see the relation between binary and ternary Ga-based chalcogenides. It is well-known that AB_2X_4 (A = Zn, Cd, Hg; B = Al, Ga, In; X = S, Se, Te) chalcogenides usually crystallize in DC (A = Cd, Hg) and DS (A = Zn) phases that are tetrahedrally coordinated structures derived from the zinc-blende structure of AX compounds. On compression, cations and vacancies in both DC or DS phases exhibit a pressure-induced cation-vacancy disorder process. This corresponds to an order−disorder PT leading to intermediate partially disordered DS phases prior to undergoing a total cation-vacancy disorder process at higher pressures when they undergo a PT to the DR phase.[81,108,112] Once the pressure is released, they cannot recover their original DC and DS phases. Instead, a DZ phase is obtained. Moreover, it has been shown that a reversible DZ-to-DR HP-PT is observed in these chalcogenides.[79,80,113−115] All this information regarding the pressure-induced order−disorder PTs in ternary OVCs was mapped by Meenakshi et al.[81] after taking into consideration the temperature-induced order−disorder PTs in OVCs.[116] Latter, Manjón et al. revised and discussed all the possible order−disorder PTs between the DC and the DZ structure in order to classify the degree of disorder in these compounds.[117]

Even though ternary AGa_2X_4 and binary Ga_2X_3 compounds do not share the same LP phases, all of them can be derived from the tetrahedrally coordinated zincblende and wurtzite structures and include a second cation and vacancies (AGa_2X_4) or just vacancies (Ga_2X_3) in cation positions. Therefore, it is clear from the above considerations that both families of Ga-based chalcogenides (Ga_2X_3 and AGa_2X_4) are OVCs that share common DZ and DR structures at LP and HP, respectively, and that phases can be obtained on compression and decompression. Therefore, considering the information already mentioned, we have reformulated the Meenakshi's scheme of HP-PTs in AGa_2X_4 compounds to include the experimental and theoretical predicted phase transitions on Ga_2X_3 sesquichalcogenides. In this way, we show that Ga_2X_3 sesquichalcogenides can also be considered as binary OVCs not only from the point of view of the behavior at HT but also at HP (Figure 9).

One difference between both families of Ga_2X_3 and AGa_2X_4 chalcogenides shown in Figure 9 is that in ternary Ga-based OVCs, all HP-PTs are order−disorder PTs, e.g., the DC-to-DR PT. However, most binary Ga-based OVCs show HP-PTs characterized by a relocation of the vacancies rather than a mixture of cations and vacancies (the exception seems to be β-Ga_2Se_3 that undergoes a PT to the DR phase). In this case, the interlayer space in φ-Ga_2S_3 and β'-Ga_2S_3 can be considered as planes of vacancies, as recently suggested in refs 99 and 109. Another difference between both families of chalcogenides is that ternary AGa_2X_4 chalcogenides only exhibit DR phases at HP (the R-$3m$ phase has never been found). This difference can be explained because in binary Ga_2X_3 compounds, the lack of a second cation allows one to obtain either the DR phase (Ga_2Se_3) or the β' phase (Ga_2S_3 and Ga_2Te_3) on compression.

In short, the HP relations emphasized in Figure 9 point out that, despite the different stoichiometry of Ga_2X_3 and AGa_2X_4 compounds and how vacancies are placed in their structures at RC, leading to somewhat different tetrahedrally coordinated structures, they finally end up sharing an octahedrally coordinated DR phase at HP as well as a tetrahedrally coordinated DZ phase on decompression. It is important to emphasized that our newly proposed scheme of pressure-induced phase transitions in Ga-based OVCs include different paths to explore: (i) the β'-φ phase transition in Ga_2Te_3, (ii) the

obtention of β'-Ga_2Se_3, and (iii) the pressure-induced phase transitions in DZ-Ga_2S_3.

5. CONCLUSIONS

In this work, we have reported HP-RS and HP-XRD measurements on α'-Ga_2S_3 (s.g. Cc) and DFT simulations of different phases on Ga_2S_3, Ga_2Se_3, and Ga_2Te_3 to identify and analyze the behavior of the HP phases of α'-Ga_2S_3 observed upon compression and decompression. We have demonstrated that the pressure-induced phase transition from α'-Ga_2S_3 to β'-Ga_2S_3 (s.g. $R\bar{3}m$, isostructural with β-In_2Se_3) occurs at ~16.0 GPa and does not require LH to occur, although additional thermal energy could ease the phase transition. The identification of all the Raman-active modes observed above 16 GPa confirms the $R\bar{3}m$ nature of β'-Ga_2S_3. Moreover, we have shown that the SM observed in β'-Ga_2S_3 comes from the A_{1g}^1−E_g^1 combination, and we have provided a hypothesis for its observation that would require one to perform HP-RS measurements at HT. On decompression, we have shown that below 9.0 GPa a new phase (φ-Ga_2S_3) with s.g. $R3m$ (isostructural with α-In_2Se_3) is attained, and their Raman-active modes have been reported. The experimental and theoretical pressure dependence of the vibrational modes and structural parameters (unit-cell volume per formula unit, zero-pressure axial compressibilities, bulk modulus, and their first pressure derivative) have allowed us to identify the nature of φ-Ga_2S_3. This $R\bar{3}m$-to-$R3m$ phase transition is also supported by the lower energy of the $R3m$ phase than the $R\bar{3}m$ structure at low pressures as evidenced by theoretical *ab initio* simulations.

According to the literature, this is the first time that a $R3m$ phase has been synthesized in Ga-based sesquichalcogenides. What is more, this implies a pressure-induced paraelectric-ferroelectric β'-φ phase transition that is similar to the temperature-induced ferroelectric-paraelectric phase transition from the α-In_2Se_3-like structure to the β-In_2Se_3-like structure predicted in III−VI sesquichalcogenides. Moreover, we have proposed a mechanism to explain the $R\bar{3}m$-to-$R3m$ phase transition on the downstroke for Ga_2S_3 that could also be valid for other III−VI sesquichalcogenides.

On the other hand, a new phase has been observed in Ga_2S_3 on the downstroke below 1.0 GPa (γ-Ga_2S_3) that remains metastable at RC. We have tentatively proposed that this phase has a DZ structure (a structure also observed at HT); however, this must still be confirmed by detailed XRD measurements. We have also proposed that γ-Ga_2S_3 is expected to show a phase transition at HP to the DR structure, as it occurs for α-Ga_2Se_3 and DZ-$CdGa_2S_4$. In this context, we have studied the different phase transitions of Ga_2S_3, Ga_2Se_3, and Ga_2Te_3 either at HT or at HP. On account of the similarities of the HT and HP phase transitions in Ga_2X_3 chalcogenides and AGa_2X_4 chalcogenides, we have reformulated the pressure-behavior scheme for AGa_2X_4 compounds by including the Ga_2X_3 chalcogenides as another kind of OVCs. In this scheme, both families share the DR phase at HP and the decompressed DZ structure either at LP or at HT, regardless of the different stoichiometries and starting structures. These shared phases can only be understood if we consider the presence of ordered vacancies in the crystalline structure of both families at room conditions.

Finally, it must be stressed that our results open new possibilities for the Ga_2S_3 system to design cheap, nontoxic, nonrare-earth, and abundant-element-based devices for SHG, PWS, ferroelectric, pyroelectric, and piezoelectric applications. Moreover, it could guide future works devoted to synthesize of

α- and β-In_2Se_3-like structures in other III−VI B_2X_3 (B = Al, Ga, In; X = S, Se, Te) chalcogenides via compression/decompression, via existing or emerging 2D materials synthesis methods, or even by PLD, as it has been recently demonstrated in β'-Ga_2Te_3.

■ ASSOCIATED CONTENT

Ⓢ Supporting Information

The Supporting Information is available free of charge at https://pubs.acs.org/doi/10.1021/acs.chemmater.2c01169.

Crystal structures, high-pressure Raman measurements, experimental and theoretical pressure dependence of the Raman frequencies, theoretical phonon dispersions, and theoretical volume dependence of the total energy (PDF)

■ AUTHOR INFORMATION

Corresponding Authors

Samuel Gallego-Parra − *Instituto de Diseño para la Fabricación y Producción Automatizada, MALTA Consolider Team, Universitat Politècnica de València, 46022 València, Spain*; Email: sagalpar@doctor.upv.es

Rosario Vilaplana − *Centro de Tecnologías Físicas, MALTA Consolider Team, Universitat Politècnica de València, 46022 València, Spain;* ⓞ orcid.org/0000-0003-0504-2157; Email: rovilap@fis.upv.es

Authors

Oscar Gomis − *Centro de Tecnologías Físicas, MALTA Consolider Team, Universitat Politècnica de València, 46022 València, Spain*

Plácida Rodríguez-Hernández − *Departamento de Física, Instituto de Materiales y Nanotecnología, MALTA Consolider Team, Universidad de La Laguna, 38207 San Cristóbal de La Laguna, Spain;* ⓞ orcid.org/0000-0002-4148-6516

Alfonso Muñoz − *Departamento de Física, Instituto de Materiales y Nanotecnología, MALTA Consolider Team, Universidad de La Laguna, 38207 San Cristóbal de La Laguna, Spain;* ⓞ orcid.org/0000-0003-3347-6518

Jesus Antonio González − *Ciencias de la Tierra y Fisica de la Materia Condensada, MALTA Consolider Team, Universidad de Cantabria, 39005 Santander, Spain*

Juan Angel Sans − *Instituto de Diseño para la Fabricación y Producción Automatizada, MALTA Consolider Team, Universitat Politècnica de València, 46022 València, Spain;* ⓞ orcid.org/0000-0001-9047-3992

Catalin Popescu − *ALBA-CELLS, MALTA Consolider Team, 08290 Cerdanyola del Valles, Barcelona, Spain*

Francisco Javier Manjón − *Instituto de Diseño para la Fabricación y Producción Automatizada, MALTA Consolider Team, Universitat Politècnica de València, 46022 València, Spain*

Complete contact information is available at:
https://pubs.acs.org/10.1021/acs.chemmater.2c01169

Notes

The authors declare no competing financial interest.

■ ACKNOWLEDGMENTS

■ REFERENCES

(1) Pardo, M.; et al. Diagramme de phases gallium-soufre et études structurales des phases solides. *J. Solid State Chem.* **1993**, *102* (2), 423−433.

(2) Tomas, A.; et al. X-ray diffraction and electron microscopy studies of α-and β-Ga_2S_3. *physica status solidi (a)* **1988**, *107* (2), 775−784.

(3) Guymont, M.; et al. Electron microscope study of γ-Ga_2S_3. *physica status solidi (a)* **1989**, *113* (1), K5−K7.

(4) Zheng, Y.; et al. Large-Size Ultrathin α-Ga_2S_3 Nanosheets toward High-Performance Photodetection. *Adv. Funct. Mater.* **2021**, *31* (6), 2008307.

(5) Jastrzebski, C.; et al. Synthesis and structural characterization of microcrystalline Ga_2S_3 layers on a GaP semiconductor substrate. *Materials Science in Semiconductor Processing* **2019**, *94*, 80−85.

(6) Kim, J.; et al. Simultaneous growth of Ga_2S_3 and GaS thin films using physical vapor deposition with GaS powder as a single precursor. *Nanotechnology* **2019**, *30* (38), 384001.

(7) Al Garni, S.; Qasrawi, A. Design and characterization of the Ge/Ga_2S_3 heterojunction. *J. Electron. Mater.* **2017**, *46* (8), 4848−4856.

(8) Zhou, N.; et al. Nonlayered two-dimensional defective semiconductor γ-Ga_2S_3 toward broadband photodetection. *ACS Nano* **2019**, *13* (6), 6297−6307.

(9) Murtaza, G.; et al. Scalable and universal route for the deposition of binary, ternary, and quaternary metal sulfide materials from molecular precursors. *ACS applied energy materials* **2020**, *3* (2), 1952−1961.

(10) Liu, H.; et al. Synthesis and phase evolutions in layered structure of Ga_2S_3 semiconductor thin films on epiready GaAs (111) substrates. *ACS Appl. Mater. Interfaces* **2014**, *6* (5), 3501−3507.

(11) Alsaif, M. M.; et al. Atomically thin Ga_2S_3 from skin of liquid metals for electrical, optical, and sensing applications. *ACS Applied Nano Materials* **2019**, *2* (7), 4665−4672.

(12) Xu, K.; et al. A high-performance visible-light-driven all-optical switch enabled by ultra-thin gallium sulfide. *Journal of Materials Chemistry C* **2021**, *9* (9), 3115−3121.

(13) Eriguchi, K.; et al. Temperature-dependent growth of hexagonal and monoclinic gallium sulfide films by pulsed-laser deposition. *AIP Advances* **2020**, *10* (10), 105215.

(14) Chandrasekaran, S.; et al. Electronic structure engineering on two-dimensional (2D) electrocatalytic materials for oxygen reduction, oxygen evolution, and hydrogen evolution reactions. *Nano Energy* **2020**, *77*, 105080.

(15) Zhou, N.; Yang, R.; Zhai, T. Two-dimensional non-layered materials. *Materials Today Nano* **2019**, *8*, 100051.

(16) Wang, F.; et al. Two-Dimensional Non-Layered Materials: Synthesis, Properties and Applications. *Adv. Funct. Mater.* **2017**, *27* (19), 1603254.

(17) Alharbi, S.; Qasrawi, A. Dielectric dispersion in Ga_2S_3 thin films. *Plasmonics* **2017**, *12* (4), 1045−1049.

(18) Zhang, M., et al. *Optical parametric oscillator and second harmonic generator using monoclinic phase Ga_2S_3 crystal*. U.S. Patent 9,766,529 B2, 2017.

(19) Zheng, F.; et al. Thermodynamic optimization of the Ga−Se system. *Calphad* **2008**, *32* (2), 432−438.

(20) Kerkhoff, M.; Leute, V. The phase diagram of the quasibinary system Ga_2Te_3/Ga_2Se_3. *Journal of alloys and compounds* **2004**, *381* (1−2), 124−129.

(21) Woolley, J.; Pamplin, B.; Holmes, P. The ordered crystal structure of In_2Te_3. *Journal of the Less Common Metals* **1959**, *1* (5), 362−376.

(22) Huang, G.-Y.; Abdul-Jabbar, N.; Wirth, B. First-principles study of the structure and band structure of Ga_2Se_3. *J. Phys.: Condens. Matter* **2013**, *25* (22), 225503.

(23) Finkman, E.; et al. Lattice dynamics of tetrahedrally bonded semiconductors containing ordered vacant sites. *Phys. Rev. B* **1975**, *11* (10), 3785−3794.

(24) Weitze, D.; Leute, V. The phase diagrams of the quasibinary systems $HgTe/In_2Te_3$ and $CdTe/In_2Te_3$. *Journal of alloys compounds* **1996**, *236* (1−2), 229−235.

(25) Huang, G.-Y.; Abdul-Jabbar, N.; Wirth, B. Theoretical study of Ga_2Se_3, Ga_2Te_3, and $Ga_2(Se_{1-x}Te_x)_3$: Band-gap engineering. *Acta Mater.* **2014**, *71*, 349−369.

(26) Dai, Z.; Ohuchi, F. Vacancy ordering of Ga_2Se_3 at GaSe/GaAs (100) interface. *Applied physics letters* **1998**, *73* (7), 966−968.

(27) Ollitrault-Fichet, R.; Rivet, J.; Flahaut, J. Le système Ga-Se et les séléniures de gallium. *J. Solid State Chem.* **1980**, *33* (1), 49−61.

(28) Liu, Y.; et al. Thermodynamic assessment of the Ga−Se−Te system. *Calphad* **2020**, *71*, 102206.

(29) Antonopoulos, J. G.; Karakostas, T.; Bleris, G. L.; Economou, N. A.; et al. On the phase diagram of the Ga-Te system in the composition range 55 at% Te. *J. Mater. Sci.* **1981**, *16* (3), 733−738.

(30) Guymont, M.; Tomas, A.; Guittard, M. The structure of Ga_2Te_3 an x-ray and high-resolution electron microscopy study. *Philosophical Magazine A* **1992**, *66* (1), 133−139.

(31) Chou, C.; et al. An ordered Ga_2Te_3 phase in the ZnTe/GaSb interface. *Journal of applied physics* **1993**, *74* (11), 6566−6570.

(32) Newman, P.; Cundall, J. Superlattice Structure in Ga_2Te_3. *Nature* **1963**, *200* (4909), 876−876.

(33) Rusu, M.; et al. Deposition and characterization of Ga_2Se_3 thin films prepared by a novel chemical close-spaced vapour transport technique. *J. Phys.: Condens. Matter* **2003**, *15* (47), 8185−8193.

(34) Ueno, K.; et al. Epitaxial growth of a vacancy-ordered Ga_2Se_3 thin film on a vicinal Si(0 0 1) substrate. *Journal of crystal growth* **2002**, *237*, 1610−1614.

(35) George, K.; et al. Telluroether and selenoether complexes as single source reagents for low pressure chemical vapor deposition of crystalline Ga_2Te_3 and Ga_2Se_3 thin films. *Chem. Mater.* **2013**, *25* (9), 1829−1836.

(36) Mutlu, I. H.; Zarbaliyev, M. Z.; Aslan, F. Preparation of Ga_2Se_3 thin films by sol−gel technique. *Journal of sol-gel science technology* **2009**, *50* (3), 271−274.

(37) Kojima, N.; et al. Ga_2Se_3 and $(InGa)_2Se_3$ as novel buffer layers in the GaAs on Si system. *AIP Conference Proceedings* **2013**, *1556*, 38−40.

(38) Li, B.; et al. Suspended Ga_2Se_3 film and epitaxial Bi_2Se_3 (221) on GaSb (001) by molecular-beam epitaxy. *J. Cryst. Growth* **2017**, *459*, 76−80.

(39) Isik, M.; Gasanly, N. Investigation of structural and optical characteristics of thermally evaporated Ga_2Se_3 thin films. *Vacuum* **2020**, *179*, 109501.

(40) Yitamben, E.; et al. Surface morphology of Cr:Ga_2Se_3 heteroepitaxy on Si (001). *Phys. Rev. B* **2009**, *80* (7), No. 075314.

(41) Su, P.-Y.; et al. Crystalline and transport properties of Ga_2Te_3 synthesized by metalorganic chemical vapor deposition. *Electronic Materials Letters* **2016**, *12* (1), 82−86.

(42) Kolobov, A.; et al. Local structure of the crystalline and amorphous states of Ga_2Te_3 phase-change alloy without resonant bonding: A combined x-ray absorption and ab initio study. *Phys. Rev. B* **2017**, *95* (5), No. 054114.

(43) Zhu, H.; et al. Ga_2Te_3 phase change material for low-power phase change memory application. *Appl. Phys. Lett.* **2010**, *97* (8), No. 083504.

(44) Al-Orainy, R. H.; et al. Thermoelectric, transport and microstructure properties of binary chalcogenide Ga_2Te_3 Crystals. *Int. Res. J. Eng. Technol.* **2015**, *2* (2), 816.

(45) Chang, H.-C.; et al. Smart assembling of multi-scaled functional interfaces in thermoelectric Ga_2Te_3/Te hetero-nanocomposites. *Nanoscale* **2014**, *6* (23), 14280−14288.

(46) Tverjanovich, A.; et al. Atypical phase-change alloy Ga_2Te_3: atomic structure, incipient nanotectonic nuclei, and multilevel writing. *Journal of Materials Chemistry C* **2021**, *9* (47), 17019−17032.

(47) Ho, C.-H. Ga_2Se_3 Defect Semiconductors: The Study of Direct Band Edge and Optical Properties. *ACS Omega* **2020**, *5* (29), 18527−18534.

(48) Hu, Y.; et al. Solid solution synthesis of $(In_{1−x}Ga_x)_2Se_3$ Nanocrystals $(0≤ x≤ 1)$ by a triethylene glycol based solution process. *Mater. Lett.* **2016**, *170*, 151−155.

(49) Valeev, R.; Kriventsov, V.; Mezentsev, N. EXAS study of the promising semiconductor material Ga_2Se_3. *Bulletin of the Russian Academy of Sciences: Physics* **2013**, *77* (9), 1154−1156.

(50) Guo, S. P.; et al. Large Second Harmonic Generation (SHG) Effect and High Laser-Induced Damage Threshold (LIDT) Observed Coexisting in Gallium Selenide. *Angew. Chem., Int. Ed.* **2019**, *131* (24), 8171−8175.

(51) Jin, H.; et al. Data-driven systematic search of promising photocatalysts for water splitting under visible light. *journal of physical chemistry letters* **2019**, *10* (17), 5211−5218.

(52) Manjón, F.; et al. High-pressure studies of topological insulators Bi_2Se_3, Bi_2Te_3, and Sb_2Te_3. *physica status solidi (b)* **2013**, *250* (4), 669−676.

(53) Popović, S.; et al. Revised and new crystal data for indium selenides. *J. Appl. Crystallogr.* **1979**, *12* (4), 416−420.

(54) Ye, J.; et al. Crystal structures and phase transformation in In_2Se_3 compound semiconductor. *Japanese journal of applied physics* **1998**, *37* (8R), 4264−4271.

(55) Osamura, K.; Murakami, Y.; Tomiie, Y. Crystal Structures of $α$- and $β$-Indium Selenide, In_2Se_3. *J. Phys. Soc. Jpn.* **1966**, *21* (9), 1848−1848.

(56) Han, G.; et al. Indium selenides: structural characteristics, synthesis and their thermoelectric performances. *Small* **2014**, *10* (14), 2747−2765.

(57) Vilaplana, R.; et al. Experimental and theoretical studies on $α$-In_2Se_3 at high pressure. *Inorganic chemistry* **2018**, *57* (14), 8241−8252.

(58) Zhao, J.; Yang, L. Structure evolutions and metallic transitions in In_2Se_3 under high pressure. *J. Phys. Chem. C* **2014**, *118* (10), 5445−5452.

(59) Ding, W.; et al. Prediction of intrinsic two-dimensional ferroelectrics in In_2Se_3 and other III_2-VI_3 van der Waals materials. *Nat. Commun.* **2017**, *8*, 14956.

(60) Hu, L.; Huang, X. Peculiar electronic, strong in-plane and out-of-plane second harmonic generation and piezoelectric properties of atom-thick $α$-M_2X_3 (M= Ga, In; X= S, Se): role of spontaneous electric dipole orientations. *RSC Adv.* **2017**, *7* (87), 55034−55043.

(61) Fu, C.-F.; et al. Intrinsic electric fields in two-dimensional materials boost the solar-to-hydrogen efficiency for photocatalytic water splitting. *Nano Lett.* **2018**, *18* (10), 6312−6317.

(62) Liu, J.; Pantelides, S. Pyroelectric response and temperature-induced $α$-$β$ phase transitions in $α$-In_2Se_3 and other $α$-III_2VI_3 (III= Al, Ga, In; VI= S, Se) monolayers. *2D Materials* **2019**, *6* (2), No. 025001.

(63) Huang, J.; et al. First-principles study of two-dimensional ferroelectrics using self-consistent Hubbard parameters. *Phys. Rev. B* **2020**, *102* (16), No. 165157.

(64) Huang, Y.-T.; et al. Mexican-hat potential energy surface in two-dimensional III_2-VI_3 materials and the importance of entropy barrier in ultrafast reversible ferroelectric phase change. *Applied Physics Reviews* **2021**, *8* (3), No. 031413.

(65) Hu, L.; Wei, D. Janus group-III chalcogenide monolayers and derivative type-II heterojunctions as water-splitting photocatalysts with strong visible-light absorbance. *J. Phys. Chem. C* **2018**, *122* (49), 27795−27802.

(66) Cai, H.; et al. Synthesis and emerging properties of 2D layered III−VI metal chalcogenides. *Applied Physics Reviews* **2019**, *6* (4), No. 041312.

(67) Shang, J.; Tang, X.; Kou, L. Two dimensional ferroelectrics: Candidate for controllable physical and chemical applications. *Wiley Interdisciplinary Reviews: Computational Molecular Science* **2021**, *11* (2), e1496.

(68) Hieu, N. N.; et al. Structural, electronic, and transport properties of quintuple atomic Janus monolayers $Ga2SX_2$ (X= O, S, Se, Te): First-principles predictions. *Phys. Rev. B* **2022**, *105* (7), No. 075402.

(69) Lai, X.; et al. Experimental and theoretical identification of a high-pressure polymorph of Ga_2S_3 with $α$-Bi_2Te_3-type structure. *J. Appl. Phys.* **2014**, *116* (19), 193507.

(70) Gallego-Parra, S.; et al. Structural, vibrational and electronic properties of $α'$-Ga_2S_3 under compression. *Phys. Chem. Chem. Phys.* **2021**, *23* (11), 6841−6862.

(71) Yang, L.; et al. High-pressure structural phase transition and metallization in Ga_2S_3 under non-hydrostatic and hydrostatic conditions up to 36.4 GPa. *Journal of Materials Chemistry C* **2021**, *9* (8), 2912−2918.

(72) Takumi, M.; et al. Structural phase transitions of Ga_2Se_3 and GaSe under high pressure. *physica status solidi* **2001**, *223* (2), 423−426.

(73) Takumi, M.; Koshio, Y.; Nagata, K. X-Ray, Raman and Photoluminescence Study of Vacancy Ordered $β$-Ga_2Se_3 under High Pressure. *physica status solidi (b)* **1999**, *211* (1), 123−129.

(74) Hong, M.; et al. Pressure-Induced Structural Phase Transition and Metallization in Ga_2Se_3 up to 40.2 GPa under Non-Hydrostatic and Hydrostatic Environments. *Crystals* **2021**, *11* (7), 746.

(75) Serebryanaya, N. The Crystal Structure of Pressure-Induced Phases of In_2Te_3 and Ga_2Te_3. *Powder Diffraction* **1992**, *7* (2), 99−102.

(76) Lu, Z.; et al. 2D materials based on main group element compounds: phases, synthesis, characterization, and applications. *Adv. Funct. Mater.* **2020**, *30* (40), 2001127.

(77) Tao, P.; et al. Recent advances in exfoliation techniques of layered and non-layered materials for energy conversion and storage. *Journal of Materials Chemistry A* **2019**, *7* (41), 23512−23536.

(78) Yuan, H.; Wang, H.; Cui, Y. Two-dimensional layered chalcogenides: from rational synthesis to property control via orbital occupation and electron filling. *Accounts of chemical research* **2015**, *48* (1), 81−90.

(79) Gallego-Parra, S.; et al. Vibrational properties of $CdGa_2S_4$ at high pressure. *J. Appl. Phys.* **2019**, *125* (11), 115901.

(80) Gomis, O.; et al. High-pressure optical and vibrational properties of $CdGa_2Se_4$: Order-disorder processes in adamantine compounds. *Journal of applied physics* **2012**, *111* (1), No. 013518.

(81) Meenakshi, S.; et al. High pressure X-ray diffraction study of $CdAl_2Se_4$ and Raman study of AAl_2Se_4 (A= Hg, Zn) and $CdAl_2X_4$ (X= Se, S). *J. Phys. Chem. Solids* **2006**, *67* (8), 1660−1667.

(82) Mao, H. K.; Xu, J. A.; Bell, P. M. Calibration of the ruby pressure gauge to 800 kbar under quasi-hydrostatic conditions. *Journal of Geophysical Research: Solid Earth* **1986**, *91* (B5), 4673−4676.

(83) Debernardi, A.; et al. Pressure dependence of raman linewidth in semiconductors. *Physica status solidi (b)* **2001**, *223* (1), 213−223.

(84) Fauth, F.; et al. The new material science powder diffraction beamline at ALBA synchrotron. *Powder Diffraction* **2013**, *28* (S2), S360−S370.

(85) Dewaele, A.; Loubeyre, P.; Mezouar, M. Equations of state of six metals above 94 GPa. *Phys. Rev. B* **2004**, *70* (9), No. 094112.

(86) Prescher, C.; Prakapenka, V. B. DIOPTAS: a program for reduction of two-dimensional X-ray diffraction data and data exploration. *High Pressure Research* **2015**, *35* (3), 223−230.

(87) Toby, B. H.; Von Dreele, R. B. GSAS-II: the genesis of a modern open-source all purpose crystallography software package. *J. Appl. Crystallogr.* **2013**, *46* (2), 544−549.

(88) Hohenberg, P.; Kohn, W. Inhomogeneous electron gas. *Physical review* **1964**, *136* (3B), B864−B871.

(89) Kresse, G.; Hafner, J. Ab initio molecular dynamics for liquid metals. *Phys. Rev. B* **1993**, *47* (1), 558−561.

(90) Blöchl, P. E. Projector augmented-wave method. *Phys. Rev. B* **1994**, *50* (24), 17953−17979.

(91) Kresse, G.; Joubert, D. From ultrasoft pseudopotentials to the projector augmented-wave method. *Physical review b* **1999**, *59* (3), 1758−1775.

(92) Perdew, J. P.; et al. Restoring the density-gradient expansion for exchange in solids and surfaces. *Phys. Rev. Lett.* **2008**, *100* (13), 136406.

(93) Perdew, J. P.; Burke, K.; Ernzerhof, M. Generalized gradient approximation made simple. *Physical review letters* **1996**, 77 (18), 3865−3868.

(94) Grimme, S.; et al. A consistent and accurate ab initio parametrization of density functional dispersion correction (DFT-D) for the 94 elements H-Pu. *J. Chem. Phys.* **2010**, 132 (15), 154104.

(95) Parlinski, K. *Computer Code Phonon*. Available from http://www.computingformaterials.com/index.html.

(96) Sans, J.; et al. Structural, vibrational, and electrical study of compressed BiTeBr. *Phys. Rev. B* **2016**, 93 (2), No. 024110.

(97) Sans, J. A.; et al. Characterization and Decomposition of the Natural van der Waals $SnSb_2Te_4$ under Compression. *Inorg. Chem.* **2020**, 59, 9900.

(98) Manjón, F.; et al. Precursor effects of the rhombohedral-to-cubic phase transition in indium selenide. *High Pressure Research* **2002**, 22 (2), 261−266.

(99) Gallego-Parra, S.; et al. Pressure-induced order−disorder transitions in $β$-In_2S_3: an experimental and theoretical study of structural and vibrational properties. *Phys. Chem. Chem. Phys.* **2021**, 23 (41), 23625−23642.

(100) Ungár, T.; et al. Correlation between subgrains and coherently scattering domains. *Powder Diffraction* **2005**, 20 (4), 366−375.

(101) Klotz, S.; et al. Hydrostatic limits of 11 pressure transmitting media. *J. Phys. D: Appl. Phys.* **2009**, 42 (7), No. 075413.

(102) Angel, R. J.; et al. Effective hydrostatic limits of pressure media for high-pressure crystallographic studies. *J. Appl. Crystallogr.* **2007**, 40 (1), 26−32.

(103) Manjón, F. J.; et al. Combined Experimental and Theoretical Studies: Lattice-Dynamical Studies at High Pressures with the Help of Ab Initio Calculations. *Minerals* **2021**, 11 (11), 1283.

(104) Lewandowska, R.; et al. Raman scattering in $α$-In2Se3 crystals. *Materials research bulletin* **2001**, 36 (15), 2577−2583.

(105) Weszka, J.; et al. Raman scattering in In2Se3 and InSe2 amorphous films. *Journal of non-crystalline solids* **2000**, 265 (1−2), 98−104.

(106) Balakrishnan, N.; et al. Epitaxial growth of $γ$-InSe and $α$, $β$, and $γ$-In2Se3 on $ε$-GaSe. *2D Materials* **2018**, 5 (3), No. 035026.

(107) Liu, L.; et al. Atomically Resolving Polymorphs and Crystal Structures of In2Se3. *Chem. Mater.* **2019**, 31 (24), 10143−10149.

(108) Grzechnik, A.; et al. Pressure-induced phase transitions in cadmium thiogallate $CdGa_2Se_4$. *J. Solid State Chem.* **2001**, 160 (1), 205−211.

(109) Da Silva, J. L.; Walsh, A.; Lee, H. Insights into the structure of the stable and metastable $(GeTe)_m(Sb_2Te_3)_n$ compounds. *Phys. Rev. B* **2008**, 78 (22), 224111.

(110) Tao, X.; Gu, Y. Crystalline−crystalline phase transformation in two-dimensional In2Se3 thin layers. *Nano Lett.* **2013**, 13 (8), 3501−3505.

(111) Bose, D.; et al. Resistivity studies on Ga_2Te_3 and In_2Te_3 under high pressures. *Mater. Lett.* **1982**, 1 (2), 61−63.

(112) Meenakshi, S.; et al. Pressure-induced phase transition in defect Chalcopyrites $HgAl_2Se_4$ and $CdAl_2S_4$. *J. Phys. Chem. Solids* **2010**, 71 (5), 832−835.

(113) Vilaplana, R.; et al. Vibrational study of $HgGa_2S_4$ under high pressure. *J. Appl. Phys.* **2013**, 113 (9), No. 093512.

(114) Vilaplana, R.; et al. Lattice dynamics study of $HgGa_2Se_4$ at high pressures. *J. Phys. Chem. C* **2013**, 117 (30), 15773−15781.

(115) Vilaplana, R.; et al. High-pressure Raman scattering study of defect chalcopyrite and defect stannite $ZnGa_2Se_4$. *Journal of applied physics* **2013**, 113 (23), 233501.

(116) Bernard, J. E.; Zunger, A. Ordered-vacancy-compound semiconductors: pseudocubic $CdIn_2Se_4$. *Phys. Rev. B* **1988**, 37 (12), 6835−6856.

(117) Manjón, F. J.; et al. Order−disorder processes in adamantine ternary ordered-vacancy compounds. *physica status solidi (b)* **2013**, 250 (8), 1496−1504.